# Elimination of senescent cells with senolytic host-directed therapy reduces tuberculosis progression in mice

List of authors.

Somnath Shee[1], Yazmin B. Martinez-Martinez[1], Benjamin Koleske[1], Shivraj Yabaji[2], Lester Kobzik[3], Igor Kramnik[2], William Bishai[1]

[1]Center for Tuberculosis Research, Johns Hopkins University, School of Medicine, Baltimore, MD, USA.

[2] The National Emerging Infectious Diseases Laboratories (NEIDL), Boston University, Boston, MA, USA.

[3] Cellecta, Inc, Mountain View, CA, USA

Short title: Senolytic therapy for TB

Keywords.

Senescence, aging, Tuberculosis, Mycobacterium, Senolytics, Dasatinib, Quercetin, Fisetin, granuloma, necrosis, SASP, DNA damage

## Abstract

By eliciting lung necrosis, which enhances aerosol transmission, *Mycobacterium tuberculosis* (*Mtb*) sustains its long-term survival as a human pathogen. In studying the human-like necrotic granuloma lesions characteristic of *Mtb*-infected *B6.Sst1S* mice, we found that lung myeloid cells display elevated senescence markers- cell cycle arrest proteins p21 and p16, the DNA damage marker γH2A.X, senescence-associated β-Galactosidase activity, and senescence-associated secretory phenotype (SASP). These markers were also elevated in *Mtb*-infected aged wild type (WT) mice but not in young WT mice. Global transcriptomics data revealed activation of pro-survival (PI3K, MAPK) and anti-apoptotic pathways in *Mtb*-infected *B6.Sst1S* macrophages. As senescent cells are long-lived, non-dividing cells that release tissue-damaging SASP, we treated *Mtb*-infected mice with a cocktail of three senolytic drugs (dasatinib, quercetin, and fisetin) designed to kill senescent cells. Senolytic drug treatment prolonged survival and reduced *Mtb* lung counts in *B6.Sst1S* and aged WT mice to a greater degree than young WT mice and concomitantly reduced lung senescence markers. These findings indicate that (1) *Mtb* infection may induce lung myeloid cells to enter a senescent state and that these cells play a causal role in disease progression, and (2) Senolytics merit consideration for human clinical trials against tuberculosis (TB).

43 **Introduction**

44 Despite the introduction of 3 new anti-tuberculosis (TB) drugs since 2012, the global TB
45 pandemic remains poorly controlled.[1] Most humans are resistant to TB and are capable
46 of limiting the bacterial growth and inflammatory damage caused by Mycobacterium
47 tuberculosis (*Mtb*) infection.[2–4] However, susceptible individuals develop active disease
48 characterized by necrotic granulomatous lung lesions that may further transform into lung
49 cavities, leading to lung damage and morbidity even with appropriate anti-TB treatment,
50 and ultimately TB transmission.[5,6] Understanding the molecular basis for failed granuloma
51 control and necrotic lesion formation is a major unmet need in TB research.

52 While it is well known that aging is a significant risk factor for progression from contained
53 *Mtb* infection to active TB disease in both high and low-level income countries,[7–11] there
54 have been relatively few studies investigating the mechanistic basis for age-associated
55 active TB.[12–20] Senescence is a rapidly expanding research discipline as many
56 investigators have sought to understand the mechanism of gradual tissue failure in age-
57 associated chronic diseases such as dementia, heart failure, arthritis, and renal failure.[21]
58 The accumulation of senescent cells is a principal mechanism of functional tissue
59 impairment in aging.[22,23] A key lesson from the senescence literature is that aged tissues
60 are populated by long-lived, non-dividing, functionally impaired senescent cells. These
61 cells release deleterious signaling molecules- collectively termed senescence-
62 associated secretory phenotype (SASP), that locally contribute to inflammation and tissue
63 failure.[24] Indeed, transplantation of isolated senescent cells led to premature aging in
64 mice.[25,26] In this context, small molecule senolytic drugs—designed to induce apoptosis

65 in the non-dividing senescent cells— prolong mice lifespans, and improve organ function
66 in humans with chronic disease.[27,28]

67 To gain insight into the factors that lead to the loss of immune containment of *Mtb*, we
68 study the *B6.Sst1S* mice, which develop human-like necrotic lung granulomas following
69 *Mtb* infection in contrast to most wild type (WT) mouse strains.[29–35] These mice harbor
70 the *Sst1S* allele, which has loss of function mutations in the Sp140 chromatin remodeling
71 protein that plays a key role in immune cell gene regulation.[36,37] Recently Kotov *et al.*
72 described a population of interstitial macrophages (IM) and plasmacytoid dendritic cells
73 (pDC) that aberrantly secrete type I IFN (associated with TB exacerbation)[38–40], are poorly
74 responsive to IFNγ and may play a key role in granuloma breakdown in the lungs of the
75 closely related Sp140$^{-/-}$ mouse strain.[41] In this paper, we report that lung myeloid cells in
76 *Mtb*-infected *B6.Sst1S* mice displayed high levels of senescence markers prior to necrotic
77 granuloma formation and subsequently appeared closely associated with non-controlling,
78 early necrotic granulomas. Similar senescence marker increases were found in *Mtb*-
79 infected aged WT C57BL/6 (B6) mice, but not young WT B6 mice. Treatment with a three-
80 drug cocktail of FDA-approved senolytic drugs to eliminate these senescent cells restored
81 containment of *Mtb* proliferation, prolonged mouse survival, and reduced senescence
82 markers. Thus, myeloid cell entry into a senescent state may drive the failure of immune
83 containment and progression to necrosis during pulmonary TB.

84

85

86

87 **Results**

88 **Elevated senescence markers *in vitro* were detected in BMDMs from *B6.Sst1S* and**
89 **aged WT B6 but not young WT B6 mice.**

90 We previously observed that TNFα exposure induced a stress response characterized by
91 overexpression of IFNβ (Supplementary Fig. 1a) and the integrated stress response (ISR)
92 in *B6.Sst1S* bone marrow-derived macrophages (BMDMs).[34,35] Because chronic ISR
93 activation is a potential driver of cellular senescence,[42,43] we tested TNFα-stimulated
94 BMDMs from young *B6.Sst1S* mice (8-12 weeks old) alongside BMDMs from young and
95 aged (>72 weeks old) WT B6 mice (Fig. 1a). Not only did *B6.Sst1S* and aged WT B6
96 BMDMs showed poorer *Mtb* H37Rv containment following TNFα stress induction than
97 young WT B6 (Fig. 1b), they also showed greater activity of senescence-associated β-
98 galactosidase (SA-βGal) than young WT B6 BMDMs, although not to the level seen with
99 etoposide, an inducer of DNA damage-mediated senescence (Fig. 1c, 1d). In addition,
100 we observed the induction of SASP genes (*Il1β, Il1α, Il6, Mmp12, Mmp13, Ccl2, Ccl8,*
101 *Pai1*) transcription in TNFα-treated *B6.Sst1S* BMDMs compared to similarly treated WT
102 B6 cells (Fig. 1e). Moreover, TNFα- treated *B6.Sst1S* BMDMs and aged WT B6 BMDMs
103 showed the presence of established biomarkers of senescence- higher levels of the
104 cyclin-dependent kinase inhibitor P16 (cell cycle arrest), phospho(S139)-H2A.X (DNA
105 damage marker) and lower protein levels of Lamin B1 (structural constituent of the
106 nuclear lamina) (Supplementary Fig. 1b), and displayed reduced cell proliferation as
107 measured by BrdU-incorporation assay (Fig. 1f) without a significant reduction in viability
108 (Supplementary Fig. 1c). In sum, TNFα-treated *B6.Sst1S* BMDMs exhibited numerous

109 markers of senescence similar to BMDMs derived from aged WT B6 mice or etoposide-
110 treated WT B6 BMDMs.

111 **Transcriptomic signatures show upregulation of senescence markers in BMDMs**
112 **and cells from non-controlling lung lesions in *B6.Sst1S* mice.**

113 Reanalysis of transcriptomic signatures in *B6.Sst1S* versus WT B6 BMDMs with and
114 without TNFα treatment (GSE99456)[35] suggested upregulation of cellular senescence
115 pathways, enhanced DNA damage responses, activation of mitotic checkpoints, pro-
116 survival ERK1/ERK2 protein kinase cascade, and cellular response to IFNβ (by
117 Metascape Analysis;[44] Supplementary Fig. 2, Supplementary File S1) in *B6.Sst1S*
118 BMDMs. To examine whether these signatures appear in the context of active lung
119 infection, we performed spatial transcriptomics to profile myeloid cells associated with
120 controlling (C) versus non-controlling (NC) lesions in *B6.Sst1S* mouse lungs (Fig. 2a). To
121 do this, we first administered $1x10^6$ CFU of *Mtb* H37Rv subcutaneously in the hock, and
122 lung samples were harvested at 14 weeks post-infection. We categorized the lesions into
123 non-controlling (NC; advanced multibacillary lesions with necrotic core) and controlling
124 (C; non-necrotic paucibacillary lesions) granulomas. We identified 734 differentially
125 expressed genes (DEGs; $\log_2$fold change>1 or <-1, adjusted $p< 0.05$) in NC vs C lesions
126 (Fig. 2b, Supplementary File S2), and functional pathway enrichment analysis[44] identified
127 inflammatory response, extracellular matrix organization, lung fibrosis and negative
128 regulation of cell proliferation pathways to be significantly higher in NC lesions
129 (Supplementary Fig. 3a). NC lesion DEGs also showed a high degree of overlap with the
130 SenMayo[45] senescence-associated gene set (Supplementary Fig. 3b, 3c). Taken
131 together, our spatial transcriptomics data further supports the association of senescence

132 markers with progression to necrotic granuloma formation in *Mtb*-infected *B6.Sst1S*
133 mouse lungs.

134 ***In vivo* senescence markers are elevated in *Mtb*-infected young *B6.Sst1S* and aged**
135 **WT B6 compared to young WT B6 mice, predominantly on myeloid cells at earlier**
136 **time points.**

137 We infected young *B6.Sst1S* and WT B6 mice, aged WT B6 mice with a low-dose *Mtb*
138 aerosol infection route (Fig. 2c). *Mtb* proliferation was significantly higher uniquely in
139 young *B6.Sst1S* mice, with necrosis appearing as early as 4 weeks post-infection (wpi)
140 (Fig. 2d, 2g). Both young *B6.Sst1S* and aged WT B6 showed increased dissemination to
141 the spleen at 6 wpi, suggesting that aged WT B6 mice have a defect in containment
142 compared to young WT B6 (Fig. 2e). At 2 wpi, when lung CFU counts were equivalent
143 across all three groups, we observed a higher degree of immunopathology as measured
144 by area of lung consolidation in the H&E-stained lungs of aged WT B6 ($p$= 0.03), and
145 *B6.Sst1S* mice showed no difference in H&E stained area than in young WT B6 mice (Fig.
146 2f, 2h). Surprisingly, at 4 wpi we observed decreased pathology in aged WT B6 mice
147 lungs (Fig. 2g, 2h).

148 To follow up on our *in vitro* BMDM findings with senescence markers, we sought to
149 determine whether markers of senescence were elevated during *in vivo* mouse infections.
150 We evaluated lung levels of γH2A.X and p21 at the 2 wpi-timepoint when no differences
151 in CFU were noted (Fig. 2d) and observed that both young *B6.Sst1S* and aged WT B6
152 mice showed qualitatively higher immunostaining for γH2A.X and p21 by IHC (Fig. 2f),
153 and these levels continued to increase at 4 wpi in *B6.Sst1S* mice but not aged WT B6
154 (Fig. 2g). Quantification of γH2A.X staining confirmed elevated levels for both *B6.Sst1S*

155 and aged WT B6 mice relative to young WT B6 mice at 2 wpi (Fig. 2i). To refine this
156 analysis, we turned to flow cytometric measurements of widely accepted senescence
157 markers (p21, p16 and SA-βGal)[46,47] with lung and spleen cells (Fig. 3a). To examine the
158 temporal relationship between senescence and elevated *Mtb* burden, we measured the
159 senescent cell populations at an early time point, 10 days post-infection (dpi) when lung
160 CFU burdens are the same across all groups (Supplementary Fig. 4a). We found that the
161 percent double positive $p16^{+}p21^{+}$ cells and the percent SA-$\beta Gal^{+}$ cells out of all live cells
162 were significantly higher in the lungs of *Mtb*-infected young *B6.Sst1S* and aged WT B6
163 mice than in young WT B6 (Fig. 3b, 3c). The elevation of senescence markers in young
164 *B6.Sst1S* and aged WT B6 mice were not seen in either uninfected lung or spleen cells
165 (Fig. 3b, 3c), likely because at 10 dpi there was little or no *Mtb* dissemination to spleen
166 (Supplementary Fig. 4b). Importantly, myeloid cells— predominantly alveolar (AM) and
167 interstitial macrophages (IM)- accounted for the majority of the enrichment in senescence
168 markers (double positive $p16^{+}p21^{+}$ cells and SA-$\beta Gal^{+}$ cells) as seen in young *B6.Sst1S*
169 and aged WT B6 mice lung cells (Fig. 3d, 3e). No differences in senescence marker
170 abundance between the three types of mice were observed for B cells, and with T cells
171 we found a modest elevation of SA-$\beta Gal^{+}$ senescence marker in aged WT B6 mice which
172 was not seen with the double positive $p16^{+}p21^{+}$ marker (Fig. 3d, 3e). Similar data were
173 observed at 20 dpi (Supplementary Fig. 5). Lastly, we evaluated lung levels of SASP
174 cytokines and found that five of the eight tested (IL-1β, IL-6, TNFα, IL-17a, and GM-CSF)
175 were significantly elevated in young *B6.Sst1S* mouse lungs compared to young WT B6,
176 although no differences were seen in aged WT B6 (Fig. 3f). Thus during *in vivo* mouse
177 infections, certain senescence markers— most notably macrophages doubly positive

178 p16$^{+}$p21$^{+}$ or for SA-βGal$^{+}$-are elevated in young *B6.Sst1S* and aged WT B6 mice
179 compared to young WT B6 mice, at a time point where no differences in CFU or pathology
180 are detected.

181 **'Omics studies identify the upregulation of pro-survival phosphatidylinositol 3-**
182 **kinase signaling (PI3K)- ERK1/2 cascade and anti-apoptotic pathways in *Mtb*-**
183 **infected BMDMs from *B6.Sst1S* mice.**

184 Senescent cells characteristically express cell cycle arrest and pro-inflammatory
185 transcriptional profiles. To compare the gene expression in stressed *B6.Sst1S* compared
186 to young WT B6 BMDMs, we performed bulk RNA- sequencing on BMDMs subjected to
187 10 ng/ml TNFα pretreatment, followed by *Mtb* infection in the continued presence of TNFα
188 (Fig. 4a). Despite increased *Mtb* proliferation in TNFα-treated *B6.Sst1S* BMDMs, cell
189 viability remained intact across all groups (Supplementary Fig. 6a, 6b). The dataset
190 revealed 1177 DEGs (*p. adj.*< 0.05, $\log_2$fold change >1 or <-1): 647 upregulated and 530
191 downregulated genes in *B6.Sst1S* relative to similarly treated WT B6 BMDMs
192 (Supplementary File S3). Gene ontology (GO) analysis for biological processes identified
193 receptor tyrosine kinase (RTK) signaling pathway (GO:0007169; *p.adj.*= 0.004), positive
194 regulation of PI3K signaling (GO:0014068; *p.adj.*= 0.005), negative regulation of cell
195 proliferation (GO:0008285; *p.adj.*= 0.02), and cellular response to interferon-β
196 (GO:0035458; *p.adj.*= 0.01) to be significantly enriched in the *B6.Sst1S* BMDMs (Fig. 4b,
197 Supplementary File S3). As expected, the genes absent in *B6.Sst1S* cells (*Sp140, Sp110*)
198 were among the top downregulated genes in *B6.Sst1S* BMDMs (Fig. 4c). Interestingly,
199 we observed cyclin-dependent kinase inhibitor *Cdkn1c,* senoantigen[48] *Gpnmb* and
200 several genes included in SenMayo[45] gene set (*Arg2, Ptger2, Iqgap2, Selplg, Mmp10,*

201 *Mmp12, Gem, Ets2*), to be upregulated in *B6.Sst1S* BMDMs (Fig. 4c). In addition to the
202 pro-survival (PI3K-ERK1/2/ MAPK cascade) and SASP expression regulatory pathways
203 (RTKs) known to be up-regulated in senescent cells, the stressed *B6.Sst1S* BMDMs
204 exhibited upregulation of anti-apoptotic genes (*Bcl2a1b, Bcl2a1d, Itga6, Tnfaip8*)
205 suggesting that these senescent cells are resistant to apoptosis, and thereby may provide
206 a growth-permissive condition for *Mtb*.

207 **A senolytic drug cocktail (DQF) improves the survival of the host in *Mtb*-infected**
208 ***B6.Sst1S* mice.**

209 A potential strategy to combat aging has been to employ senolytic drugs designed to kill
210 senescent cells and reverse their SASP-mediated local deleterious effects. Indeed,
211 several senolytic drugs have been shown to prolong lifespan in rodent models,[49] and
212 reduce age-associated disease morbidity in human clinical trials.[21,50–53] We selected a
213 cocktail of three most prevalent senolytic agents: dasatinib (D), quercetin (Q), and fisetin
214 (F).[54] Dasatinib is a tyrosine kinase inhibitor active against Src family and other tyrosine
215 kinases.[55] Inhibiting multiple kinases promotes apoptotic cell death in senescent cells by
216 disrupting pro-survival signaling networks such as the PI3K-ERK1/2- MAPK pathway.[49]
217 Quercetin and fisetin are flavonoid antioxidants found in common fruits and vegetables;
218 they inhibit both the anti-apoptotic BCL-2 pathway and the pro-survival PI3K-ERK1/2
219 pathway.[56–59] Since these pathways are upregulated in *Mtb*-infected *B6.Sst1S*
220 macrophages (Fig. 4b, 4c), we reasoned that targeting these pathways by the DQF
221 cocktail may alleviate *Mtb*-induced pathology in mice.

222 First, we confirmed that D, Q, and F do not exert direct anti-microbial activity against *Mtb*
223 at pharmacologically relevant concentrations (Supplementary Fig. 7a, 7b). We then

224 evaluated the host-directed effect of DQF alone or DQF in combination with partial
225 antimicrobial therapy comprised of ethambutol and rifampicin (DQF + Eth/Rif + Eth)
226 following an aerosol *Mtb* infection (Supplementary Fig. 8a). Three weeks post-infection,
227 when the lung CFU burden was 7.18 $\log_{10}$CFU units (Supplementary Fig. 8b), young
228 *B6.Sst1S* mice were randomly apportioned to four oral gavage treatment groups for a
229 period of 28 days: (i) vehicle, (ii) DQF (d21-49), (iii) Eth/Rif (d21-28) + Eth (d29-49) and
230 (iv) DQF (d21-49) +Eth/Rif (d21-28) + Eth (d29-49) (Supplementary Fig. 8a). Compared
231 with vehicle, mice receiving DQF alone showed a trend towards prolonged survival in a
232 subset of mice ($p$= 0.09) with some degree of weight stabilization (Fig. 5a, 5b). Mice
233 receiving DQF and partial antimicrobial therapy (DQF +Eth/Rif + Eth) showed a median
234 time to death (MTD) of 98 days and displayed significantly more weight gain in
235 comparison to those receiving partial antimicrobial therapy alone (Eth/Rif + Eth, MTD of
236 68 days, $p$= 0.05) (Fig. 5a, 5b). As has been noted by our group and others, [31,35,37,60]
237 *B6.Sst1S* mice display a bimodal mortality curve irrespective of therapeutic intervention
238 with these challenge doses within all groups, with 40-50% of all animals succumbing over
239 the first 35 days, and thus the impact of our drug regimens was only apparent in the
240 remaining 50-60% of surviving mice.

241 **The DQF senolytic drug cocktail reduces *Mtb* proliferation to a greater degree in**
242 **young *B6.Sst1S* and aged WT B6 mice than in young WT B6 mice.**

243 Next, we evaluated the anti-TB effect of the DQF cocktail with or without ethambutol
244 antimicrobial therapy in a lung CFU burden study of young *B6.Sst1S*, aged WT B6, and
245 young WT B6 mice following *Mtb* aerosol challenge. Because we had previously observed
246 poorer containment of *Mtb* proliferation in BMDMs from young *B6.Sst1S* and from aged

247 WT B6 mice compared to young WT B6 mice, we started drug treatment at 2 wpi for
248 young *B6.Sst1S* and aged WT B6 mice, and at 4 wpi in young WT B6 mice (Fig. 5c).
249 Compared to the vehicle-treated group, DQF therapy significantly reduced lung CFU
250 counts in *B6.Sst1S* mouse lungs by 1.3 ($p$= 0.03) and 2.2 ($p$= 0.05) $\log_{10}$CFU units at 5
251 and 8 wpi, respectively, and in aged WT B6 mouse lungs by 0.5 ($p$= 0.11) $\log_{10}$ units at 5
252 wpi (Fig. 5d). We did not find a detectable difference in lung CFU counts of young WT B6
253 mice at 8 wpi (Fig. 5d). The addition of DQF to ethambutol significantly lowered lung CFU
254 counts in all mouse strains compared to ethambutol alone, however, the magnitude of the
255 reduction was most profound in *B6.Sst1S* mice at 0.31 and 1 $\log_{10}$CFU units at 5 and 8
256 wpi, respectively, and in aged WT B6 mice at 0.6 $\log_{10}$CFU units at 5 wpi compared to
257 young WT B6 mice (Fig. 5d). Young WT B6 mice showed minimal changes with a
258 reduction of only 0.3 $\log_{10}$CFU units at 8 wpi upon adding DQF to ethambutol (Fig. 5d).
259 With spleen CFU counts, the addition of DQF to ethambutol lowered bacterial burden in
260 *B6.Sst1S* mice by 1.0 ($p$= 0.16) and 0.6 ($p$=0.05) $\log_{10}$CFU units at 5 and 8 wpi,
261 respectively, and in aged WT B6 mice by 1.1 ($p$= 0.06) $\log_{10}$CFU units at 5 wpi compared
262 to ethambutol alone (Fig. 5e). There was no significant reduction observed between these
263 groups for young WT B6 mice (Fig. 5e).

264 **The DQF cocktail reduces lung pathology and senescence markers in *Mtb*-infected**
265 **lungs of young *B6.Sst1S* and aged WT B6 mice.**

266 To determine if the improved survival and *Mtb* containment observed in DQF-treated mice
267 correlated with the removal of senescent cells, we evaluated markers of lung damage
268 and senescence in these same mouse strains (Fig. 5c) treated with DQF in the presence
269 or absence of ethambutol. Considering overall lung immunopathology, as measured by

270 the area of consolidated lesions on H&E histology slides, all three mouse strains showed
271 greater reductions with DQF+ Eth as compared with Eth alone (*B6.Sst1S*: $p$= 0.02, aged
272 WT B6: $p$= 0.13, and young WT B6: $p$= 0.26), and the overall degree of lung consolidation
273 remaining (% lesion area) was lower in young *B6.Sst1S* (5 wpi- 8.4%, 8 wpi- 9.5%) and
274 aged WT B6 mice (5 wpi- 15.4%) receiving this maximal treatment (DQF+ Eth) than in
275 young WT B6 (8 wpi) mice (26.6%) (Fig. 6a, Supplementary Fig. 9a-c, 10a).
276 Immunohistochemistry for the DNA damage marker γH2A.X showed a significant
277 reduction in DQF+ Eth- treated *B6.Sst1S* and aged WT B6 mice with mice receiving both
278 drugs showed a near absence of immunoreactivity (Fig. 6b, Supplementary Fig. 10b).
279 More notably when we evaluated live lung cells by flow cytometry for dual staining with
280 $p21^{+}\beta Gal^{+}$ and for $p16^{+}\beta Gal^{+}$, there were significant reductions in both pairs of
281 senescence markers with adding DQF alone or with DQF+ Eth in young *B6.Sst1S* and
282 aged WT B6 mice (Fig. 6c, Supplementary Fig. 10c). The lung cells showing the highest
283 reductions in dual positivity for p21+βGal+ or for p16+βGal+ were from the myeloid
284 lineage (Fig. 6d, 6e). Interestingly, Eth monotherapy also decreased the senescent cell
285 population in *B6.Sst1S* mice ($p$< 0.0001) and aged WT B6 mice ($p$= 0.08-0.09), indicating
286 that inhibiting *Mtb* replication can also impede the generation of senescent cells (Fig. 6c).
287 In contrast, we saw no changes for dual positivity in young WT B6 mice with any of the
288 DQF and/or Eth regimens compared to vehicle (Fig. 6c).

289 In sum, we observed that the senolytic drug cocktail DQF prolonged survival and reduced
290 mouse lung CFU counts with a concomitant reduction in senescence markers and
291 pathology, with TB-susceptible young *B6.Sst1S* and aged WT B6 mice generally showed
292 the largest changes compared with young WT B6.

293 **Discussion**

294 This study provides proof of concept data that lung myeloid cells acquire a senescence
295 phenotype during TB and that these senescent cells are causal drivers of disease
296 progression. In this work, we used BMDMs from aged WT B6 mice as well as young mice
297 to establish that TNFα treatment in aged and *B6.Sst1S* BMDMs are not only associated
298 with poorer *Mtb* containment but also the induction of classic senescence markers
299 including SA-βGal and SASP gene expression, cell cycle arrest (reduced BrdU
300 incorporation, Lamin B1 and increased p16), and DNA damage (γH2A.X). Our previous
301 work with the *B6.Sst1S* macrophages revealed up-regulation of many SASP genes (*Il6,*
302 *Ccl2, Cxcl11, Tgfβ3, Mmp13, Tnfsf10*) (Supplementary File S1) and induction of the anti-
303 apoptotic ISR pathway after TNFα- stimulation at an early time point (18 hours).[35] Using
304 *Mtb*-infected aged WT B6 mice as a benchmark model of senescence during TB, we
305 sought to determine whether young *B6.Sst1S* mice resembled aged WT B6 or young WT
306 B6. Our studies revealed that both young *B6.Sst1S* mice and their BMDMs displayed the
307 same panel of senescence markers during stress or *Mtb* infection as observed in aged
308 WT B6 samples. The senescence phenotypes seen in the *B6.Sst1S* model resembled
309 those of aged WT B6 samples to a much greater degree than those of young WT B6.
310 These data suggest that the *B6.Sst1S* mouse may serve as an accelerated model of
311 myeloid cell senescence exhibiting canonical senescence markers γH2A.X, p16, p21, and
312 SA-βGal activity alongside SASP enrichment in TB.

313 Advanced age is a well-known TB risk factor,[7,62,63]early mouse studies by Orme and
314 Turner showed that *Mtb*-infected old mice have accelerated lethality post-*Mtb*
315 challenge.[14,61,62] The macrophages in aged mice were *Mtb*-infected in higher numbers

316 and expressed higher levels of the IFN-I responsive genes IRGM-1 and IRF-1.[63]
317 Interestingly, DiNardo *et al.* recently found that active TB leads to accelerated aging in
318 humans and in a guinea pig acute TB model using the DNA methylation clock.[64,65] Using
319 combined hypermethylation and gene expression clock algorithms, they found that active
320 TB adds 12.7 years (by the Horvath DNA hypermethylation clock) or 14.4 years (by the
321 Transcriptomic 'RNAAgeCalc' clock) of cellular aging compared to latent TB-infected
322 humans (LTBI).[64] Consistent with this, TB patients have been reported to show
323 significantly shorter telomere length and increased mitochondrial DNA copy number
324 (markers of senescence) relative to healthy controls in a diverse population.[66–68]
325 Additional studies have indeed demonstrated that *Mtb* infection induces DNA damage,
326 manipulates host cell cycle checkpoints, and promotes senescence-like features in
327 macrophages,[69–72] or T cells.[73]
328 The senescence literature has demonstrated that pathways required for homeostatic
329 development and wound healing in young age become dysregulated during aging.[27]
330 These include fibrosis with stem cell exhaustion in the setting of chronic mTOR activation,
331 persistent inflammation with excessive SASP cytokine release due to chronic NF-κB
332 activation, and DNA damage and mitochondrial dysfunction in the setting of declining
333 sirtuin activity.[74,75] A hallmark of senescent cells is entry into a non-dividing, long-lived
334 state with chronic expression of locally deleterious signals that promote age-associated
335 disease processes. In TB, the majority of infected humans adequately contain *Mtb*
336 infection within immune-balanced quiescent lung granulomas. Our study lends support to
337 the hypothesis that failed *Mtb* containment and progression to active TB may be promoted

338 by the presence of non-dividing senescent lung myeloid cells which may suppress the
339 necessary homeostatic immune containment required for TB control.

340 We found that senescence markers in aged WT B6 and young *B6.Sst1S* appear as
341 early as 10 days after *Mtb* infection, well before the appearance of granuloma formation
342 and lung immunopathology. This early chronology suggests that myeloid cell senescence
343 may drive the more severe TB pathology in aged WT B6 and young *B6.Sst1S* animals.
344 To establish causality, we used a cocktail of the senolytic drugs DQF- which eliminate
345 senescent cells by inhibiting the kinase (RTK/ PI3K/ ERK)-dependent survival pathways
346 and anti-apoptotic mechanisms that sustain their long-lived, non-dividing state. These
347 drugs have been shown to prolong lifespan in rodents and to prevent the progression of
348 age-associated diseases in humans.[21,49–51] We found that the DQF cocktail with or without
349 partial antimicrobial therapy was sufficient to prolong mouse survival and reduce *Mtb*
350 organ burden. Moreover, the impact of the senolytic DQF cocktail was more prominent in
351 mice that showed elevated senescence markers during *Mtb* infection, specifically young
352 *B6.Sst1S* and aged WT B6 mice. The fact that senolytic drugs improve TB disease
353 outcome parameters is a potent argument that senescent lung myeloid cells are causal
354 drivers of TB progression in these animal models. As major risk factors for TB (age,
355 malnutrition, diabetes, pollution, and smoking) have been shown to induce senescence,
356 [62,76–81] our evidence that senescent cells drive TB progression may also offer a
357 mechanistic link for how these risk factors promote TB progression.

358 Considerable recent attention has been directed to the problem of post-TB lung disease.
359 Despite adequate and durable cures, many TB patients are left with serious pulmonary
360 disease, including bronchiectasis and either obstructive or restrictive lung disease.[82–85]

361 Senescent cells have been strongly associated with chronic tissue inflammation and
362 inappropriate fibrotic scarring.[86] Our studies with senolytic drugs indicated that lung
363 immunopathology was reduced to a greater degree by senolytic drugs in young *B6.Sst1S*
364 and aged WT B6 mice, which have high senescent cell burdens. Thus, in addition to
365 serving as promising adjunctive host-directed therapies for active TB, senolytic drugs may
366 also reduce post-TB lung disease.

367 In sum, by demonstrating the efficacy of Senolytics in reducing senescent cell burden
368 and improving TB outcomes in our preclinical model, we provide the rationale for testing
369 senescence-targeting strategies in human TB clinical trials.

370

371

372

373

374

375

376

377

378

379

380

381 **Material and Methods**

382 **Animals used in this study.**

383 Young C57BL/6J female mice (6 weeks old; Strain: 000664) and Aged C57BL/6J females
384 (>68 weeks old) were bought from The Jackson Laboratory (Bar Harbor, ME, USA). The
385 B6.C3H-sst1(B6J.C3-sst1C3HeB/FejKrmn) congenic mice were generated previously by
386 transferring the *sst1S* allele from C3HeB/FeJ mouse strain to the B6 (C57BL/6J) genetic
387 background using 12 backcrosses (*B6.Sst1S*)[29,35] and confirmed by Genotyping. The
388 oligonucleotides used for the PCR are shown in Supplementary Table 1. This mice strain
389 was bred and maintained at the Rodent Vivarium of Johns Hopkins University, School of
390 Medicine and was used in this study. All experiments were conducted under protocols
391 approved by the Johns Hopkins Animal Care and Use Committee (Protocol Number:
392 MO22M466) and followed established ethical animal handling and care guidelines.
393 Animals were housed in individually ventilated cages under controlled conditions,
394 including a 12-hour light/dark cycle, ambient temperatures ranging from 20 to 24°C, and
395 relative humidity between 45% and 65%. Each cage contained no more than five mice of
396 the same strain/sex to ensure proper animal welfare. Mice were randomly assigned to
397 experimental groups to minimize bias. Humane and painless euthanasia procedures were
398 employed in compliance with AVMA (American Veterinary Medical Association)
399 guidelines.

400 All experiments involving *Mycobacterium tuberculosis* H37Rv were conducted in
401 Biosafety Level 3 (BSL3) and Animal Biosafety Level 3 (ABSL3) facilities at the Johns
402 Hopkins University, School of Medicine, following protocols approved by the Institutional
403 Biosafety Committee. Aerosol infections were performed using a Glas-Col aerosolization

404 system, allowing the mice to move freely in the chamber and minimizing stress or
405 discomfort. Anesthesia was not required for this procedure. Mice were briefly restrained
406 during oral gavage to ensure accurate delivery. Infected animals were monitored for signs
407 of illness, such as weight loss or lethargy, and those that became moribund before the
408 experiment's conclusion were promptly euthanized, except in survival studies.

409 **BMDMs isolation, culture, and treatment with murine-TNFα.**

410 BMDMs were isolated from mice at the indicated age, as described previously[87]. Briefly,
411 BMDMs were isolated from the tibias and femurs of mice and were differentiated into
412 macrophages in RPMI-Glutamax (Thermo Fisher Scientific; 61870127) containing 10%
413 heat-inactivated FBS (Millipore Sigma, Catalog no.- F4135), 1X antibiotic-antimycotic
414 Solution (Sigma Aldrich; A5955) and 10% (v/v) L929 fibroblast-conditioned medium (as a
415 source of M-CSF(macrophage colony-stimulating factor)) for 5 days. L929 fibroblast cell
416 lines were cultured in DMEM-Glutamax (Thermo Fisher Scientific; 10566016) containing
417 10% heat-inactivated FBS, 10 mM HEPES, and 1X antibiotic- antimycotic Solution. L929
418 cells were mycoplasma-negative (Venorgem Mycoplasma detection kit; Millipore Sigma-
419 MP0025). BMDMs were either left untreated or treated with 10 ng/ml of murine-TNFα
420 (Peprotech; 315-01A) in RPMI-Glutamax containing 10% heat-inactivated FBS and 10%
421 (v/v) L929 fibroblast-conditioned medium, for indicated time durations at 37°C in 5% $CO_2$.
422 BMDMs were washed, scraped out, counted, and replated overnight prior to the
423 experiments. All experiments were done with confluency of BMDMs 60-75%.

424 **Senescence associated β-Galactosidase assay (SA-βGal assay).**

425 SA-βGal assays at indicated time points were done with both paraformaldehyde- fixed
426 (Senescence Cells Histochemical Staining Kit; Sigma; CS0030) and live BMDMs
427 (Senescence β-Galactosidase Activity Assay Kit (Fluorescence, Flow Cytometry); Cell
428 Signaling Technology; 35302), using a modified manufacturer's protocol. At indicated time
429 points, BMDMs were washed twice with PBS and fixed with 1X fixation buffer for 10
430 minutes. BMDMs were washed thrice, the staining mixture was added to each well and
431 incubated for 48 h at 37°C without $CO_2$. We used 0.04X the X-gal Solution (10 µl in 1ml
432 of Staining mixture), to avoid saturation of the signal. The plate was sealed with Parafilm
433 to prevent evaporation of the staining mixture. After the incubation, cells were observed
434 under a bright field microscope and images were captured from the center of the well. For
435 experiments with live cells, adherent BMDMs were washed twice with warm PBS, and
436 incubated in Bafilomycin A1 (freshly prepared; 100 nM) containing complete RPMI
437 medium for 2 hours. Next, 0.05X of the recommended concentration of the SA-βGal
438 Substrate Solution (0.66 µM) was added to the cells and incubated for another 2- 2.5
439 hours at 37°C and 5% $CO_2$. The cells were washed thrice with PBS, scraped out in 1ml
440 RPMI (without phenol red) (Gibco; 11835), and LIVE/DEAD Fixable Near-IR Dead Cell
441 Stain (Thermo Fisher Scientific; L10119) was added for the detection of dead cells. FACS
442 was immediately done using CytoFLEX cytometer (Beckman Coulter), and 10000
443 events/sample were recorded. BMDMs from aged WT B6 mice (>72 weeks) were used
444 as a positive control. For etoposide (Millipore Sigma; E1383)- induced senescence
445 control, WT B6 BMDMs were treated with 10 µM etoposide for 2 days in complete RPMI
446 media, followed by washing to remove DNA-damaging molecules, and further incubation

447 for 2 days, in complete RPMI media only (no loss of viability under these conditions, as
448 detected by Alamar HS assay).

449 **Cell viability assay.**

450 The viability of cells was measured using an Alamar Blue HS Cell Viability Reagent
451 (Thermo Fisher Scientific; A50100), according to the manufacturer's protocol. Briefly, at
452 the indicated point, the (warmed) viability reagent was added to each well at 1/10$^{th}$ the
453 volume of cells, incubated for 6-8 hours and the fluorescence intensity was measured
454 using a FLUOstar Omega Multidetection Microplate Reader (BMG Labtech) in the bottom-
455 reading mode with excitation at 544 nm and emission at 590 nm. Untreated cells and cells
456 treated with 0.06% SDS, were used as positive and negative control, respectively.
457 Percent viability was calculated from the relative fluorescence units compared with
458 positive and negative control cells, to which the experimental values were normalized.

459 **Isolation of RNA and quantitative RT-PCR analysis to detect SASP expression.**

460 At the indicated time points, BMDMs were lysed in TRIzol (Thermo Fisher Scientific;
461 15596026), and RNA was extracted using Qiagen RNeasy Mini Kit (74104) and RNase-
462 free DNase Set (Qiagen; 79254), following the manufacturer's protocol. RNA purity and
463 concentration were quantified using Nanodrop One (Thermo Fisher Scientific). 1 µg of
464 RNA was used for cDNA synthesis using the iScript cDNA Synthesis Kit (BioRad;
465 1708891) and quantitative RT-PCR was done with QuantStudio 3 (Applied Biosystems;
466 Thermo Fisher Scientific) using gene-specific primers (Supplementary Table 1) and iTaq
467 Universal SYBR Green Supermix (BioRad; 1725121). Expression of genes was
468 normalized with Ct value for *ActB* (internal housekeeping control).

469 **BrdU Cell proliferation assay.**

470 The capacity of BMDMs to proliferate was measured by using the BrdU Cell Proliferation
471 Assay Kit (Cell Signaling Technology; 6813), following the manufacturer's protocol.
472 Briefly, 1-day post seeding of 50000 BMDMs in a 48-well plate, growth media (RPMI-
473 Glutamax+ FBS) was removed, and RPMI-only was added to the cells to synchronize
474 their cell cycle (upon serum starvation) and incubated for 18 hours at 37°C and 5% $CO_2$.
475 After this synchronization-step, complete RPMI media was added to all wells and
476 incubated for another 24 hours. The cells were either left untreated or treated with 10ng/ml
477 TNFα, and BrdU incorporation into the cells was measured following the manufacturer's
478 recommendations. Treatment of WT B6 BMDMs with 10 μM etoposide acted as a positive
479 control. Absorbance at 450 nm was measured using the Bio-Rad iMark microplate reader.

480 **Protein isolation and Western Blotting.**

481 BMDMs were washed twice with ice-cold PBS, and the total protein was extracted by
482 lysing cells in radioimmunoprecipitation (RIPA) Buffer (Millipore Sigma; R0278) containing
483 Protease/Phosphatase Inhibitor Cocktail (1X; Cell Signaling Technology; 5872). After
484 incubating on ice for 15 min with gentle vortexing, the lysates were centrifuged at 14000
485 RPM, 4°C for 15 min. The clarified supernatant was taken, and protein concentrations
486 were quantified using the BCA Assay kit (Thermo Fisher Scientific; 23225). Approximately
487 50 μg of protein were mixed with Laemmli sample buffer (Bio-Rad; 1610747) and heated
488 at 95 °C for 5 min before loading onto 4-15% MP TGX polyacrylamide Gel (Bio-Rad;
489 45610848) and transferring to the PVDF membranes (Bio-Rad; 1620177). The PVDF
490 membranes were blocked using 5% Blotting-grade blocker (Bio-Rad; 1706404) in TBST
491 buffer- Tris-buffered saline (Quality Biological; 351086101)+ 0.1% Tween 20 (Sigma;

492 P2287) for 1-2 hour and incubated overnight at 4ºC with the primary antibodies from
493 Mouse Reactive Senescence Marker Antibody Sampler Kit (Cell Signaling Technology-
494 78551)- Phospho-Histone H2A.X (Ser139) (20E3) Rabbit mAb (1: 1000 dilution), Lamin
495 B1 (E6M5T) Rabbit mAb (1: 1000 dilution), HMGB1 (D3E5) Rabbit mAb (1: 1000 dilution),
496 p16 INK4A (E5F3Y) Rabbit mAb (1: 1000 dilution) and β-Actin (D6A8) Rabbit mAb (Cell
497 Signaling Technology; 8457) (1:5000 dilution). Following three 15 min washing steps with
498 TBST, the membranes were incubated with secondary antibody- Anti-rabbit IgG, HRP-
499 linked Antibody (1:1000 dilution) for 2 hours at room temperature (RT). Following three
500 15 min washing steps, the membranes were developed with Pierce™ ECL Western
501 Blotting Substrate (Thermo Fisher Scientific; 32109) and visualized using a KwikQuant
502 Digital Western Blot Detection System (Kindle Bioscience; D1001). Images were
503 processed in Adobe Photoshop Software. Stripping Buffer (Restore™ Western Blot
504 Stripping Buffer; Thermo Fisher Scientific; 21059) was used to redevelop PVDF
505 membranes, following the manufacturer's protocol.

506 **Bulk RNA-Sequencing and analysis.**

507 BMDMs were lysed in TRIzol (Thermo Fisher Scientific; 15596026), and RNA was
508 extracted using Qiagen RNeasy Mini Kit (74104) and RNase-free DNase Set (Qiagen;
509 79254), following the manufacturer's protocol. RNA purity and concentration was
510 quantified using Nanodrop One (Thermo Fisher Scientific) and stored at -80 ºC. RNA
511 samples were shipped on dry ice to Genewiz, Azenta Life Sciences (South Plainfield, NJ,
512 USA) for standard bulk RNA- sequencing and downstream analysis. Sample QC, library
513 preparations, sequencing reactions, and initial bioinformatic analysis were conducted as
514 follows: Total RNA samples were quantified using Qubit 2.0 Fluorometer (Life

515 Technologies, Carlsbad, CA, USA) and RNA integrity was checked with 4200 TapeStation
516 (Agilent Technologies, Palo Alto, CA, USA). Samples were initially treated with TURBO
517 DNase (Thermo Fisher Scientific, Waltham, MA, USA) to remove DNA contaminants. The
518 next steps included performing rRNA depletion using QIAseq® FastSelect™−rRNA HMR
519 kit (Qiagen, Germantown, MD, USA), which was conducted following the manufacturer's
520 protocol. RNA sequencing libraries were generated with the NEBNext Ultra II RNA Library
521 Preparation Kit for Illumina by following the manufacturer's recommendations. Briefly,
522 enriched RNAs were fragmented for 15 minutes at 94°C. First strand and second strand
523 cDNA were subsequently synthesized. cDNA fragments were end-repaired and
524 adenylated at 3'ends, and universal adapters were ligated to cDNA fragments, followed
525 by index addition and library enrichment with limited cycle PCR. Sequencing libraries
526 were validated using the Agilent Tapestation 4200 (Agilent Technologies, Palo Alto, CA,
527 USA), and quantified using Qubit 2.0 Fluorometer (ThermoFisher Scientific, Waltham,
528 MA, USA) as well as by quantitative PCR (KAPA Biosystems, Wilmington, MA, USA). The
529 sequencing libraries were multiplexed and clustered on one lane of a flow cell. After
530 clustering, the flow cell was loaded on the Illumina HiSeq 4000 instrument according to
531 the manufacturer's instructions. The samples were sequenced using a 2x150 Pair-End
532 (PE) configuration. Image analysis and base calling were conducted by HiSeq Control
533 Software (HCS). Raw sequence data (.bcl files) generated from Illumina HiSeq was
534 converted into FASTQ files and de-multiplexed using Illumina's bcl2fastq 2.17 software.
535 One mismatch was allowed for index sequence identification.

536 Raw sequencing reads were trimmed to remove adapter sequences and low-quality
537 bases using Trimmomatic v0.36, and the filtered reads were aligned to the *Mus musculus*

538 GRCm38 reference genome (ENSEMBL) using the splice-aware STAR aligner v2.5.2b,
539 generating BAM files. Gene hit counts were quantified using featureCounts from the
540 Subread package v1.5.2, counting only uniquely mapped reads overlapping annotated
541 exon regions, with strand specificity applied where appropriate. Differential expression
542 analysis was performed using the DESeq2 package[88]. Genes with an adjusted *p*-value
543 <0.05 and a $\log_2$ fold change > 1 or <-1 were deemed differentially expressed between
544 groups. Statistically significant differentially expressed genes (DEGs) were analyzed for
545 biological process enrichment through gene ontology analysis using the software
546 GeneSCF v1.1-p2 with the MGI GO database, generating clusters of functionally relevant
547 GO terms. Raw data were deposited in NCBI's Gene Expression Omnibus (GEO,
548 accession number-GSE292458). Reviewers can access this data using the following
549 token number- ihyhoqmkbhwxxmp.

550 **Minimum inhibitory concentration (MIC) and Minimum bactericidal concentration**
551 **(MBC) determination against *Mycobacterium tuberculosis* H37Rv.**

552 *Mycobacterium tuberculosis* strain H37Rv (*Mtb*) was obtained from the Johns Hopkins
553 University, Center for Tuberculosis Research (CTBR) and sequence-verified regularly.
554 *Mtb* was grown in 7H9 broth supplemented with 0.2% glycerol, 0.05% Tyloxapol (Millipore
555 Sigma; T0307), and OADC (BD; 212351) with shaking at 180 rpm in a rotary shaker
556 incubator or on 7H11 agar supplemented with OADC at 37°C. MIC was determined by a
557 resazurin microtiter assay (REMA) using 96-well flat-bottom plates[89]. *Mtb* H37Rv was
558 cultured in 7H9+OADC medium and grown to an exponential phase (optical density at
559 600 nm = 0.6-0.8). Approximately $1 \times 10^5$ bacteria per well were added in a total volume
560 of 200 µL of 7H9+OADC medium. Wells lacking *Mtb* served as controls. Additional

561 controls consisted of wells containing *Mtb* cells without drug treatment (growth control).
562 After 5 days of incubation at 37°C in the presence of drugs, 30 µL of 0.02% resazurin
563 (Sigma-Aldrich; R7017) was added, and plates were incubated for an additional 24-48
564 hours. The fluorescence intensity was measured using a FLUOstar Omega Multidetection
565 Microplate Reader (BMG Labtech) in the bottom-reading mode with excitation at 544 nm
566 and emission at 590 nm. Percent inhibition was calculated from the relative fluorescence
567 units compared with an untreated control culture; the MIC was taken as the lowest drug
568 concentration that resulted in at least 90% reduction in fluorescence compared to the
569 untreated growth control. To determine the MBC, 20 µl of cells from the respective MIC
570 dilutions (from the 96-well plate) were added onto the 7H11+OADC agar plate. Following
571 8-10 days of incubation at 37 °C, the colonies were checked for *Mtb* growth. Three wells
572 each from media containing no inoculum and, media containing *Mtb* but no drug, were
573 used as blank and growth controls, respectively. MBC was defined as the lowest drug
574 concentration at which no *Mtb* colonies appeared on the 7H11 plates.

575 **Spatial Transcriptomics of Lung from *Mtb* infected *B6.Sst1S* mice.**

576 To characterize gene expression in controlled vs uncontrolled lesions, we performed
577 spatial transcriptomics analysis using the Nanostring GeoMX Digital Spatial Profiler
578 (DSP) system (Nanostring, Seattle, WA).[90,91] The lung sections we processed for spatial
579 transcriptomics were obtained from *B6.Sst1S* mice. We used $10^6$ CFU of *Mtb* H37Rv for
580 infection, administered subcutaneously in the hock. The samples were collected at 14
581 weeks post-infection. Based on routine hematoxylin and eosin histopathology, we
582 selected lungs from 2 mice with paucibacillary controlled lesions and 2 mice with
583 advanced uncontrolled multibacillary lesions with necrotic areas. Additional FFPE

584 sections were stained with fluorescent CD45-, pan-keratin-specific antibodies and DAPI.
585 Diseased regions of interest (ROI) were selected to focus on myeloid-rich areas avoiding
586 necrosis and tertiary lymphoid tissue. Eight ROI each of controlled and uncontrolled
587 lesions (respectively) were studied. The profiling used the Mouse Whole Transcriptome
588 Atlas (WTA) panel which targets ~21,000+ transcripts for mouse protein coding genes
589 plus ERCC ( External RNA Controls Consortium) negative controls to profile the whole
590 transcriptome, excluding uninformative high expressing targets such as ribosomal
591 subunits.

592 Samples from each ROI were packaged into library for sequencing (NextSeq550,
593 Illumina) following the procedure recommended by Nanostring. After sequencing, the
594 data analysis workflow began with QC evaluation of each ROI based on thresholds for
595 number of raw and aligned reads, sequencing saturation, negative control probe means,
596 and number of nuclei and surface area. Background correction is performed using
597 subtraction of the mean of negative probe counts. Q3 normalization (recommended by
598 Nanostring) results in scaling of all ROIs to the same value for their 3rd quartile value.
599 Statistical analysis was then performed to identify differentially expressed genes, using
600 an unpaired t-test with Benjamini-Hochberg adjustment for *p* values. Raw data were
601 deposited in NCBI's Gene Expression Omnibus (GEO, accession number- GSE292392).
602 Reviewers can access this data using the following token number- clozaycmjjivduj.

603 **Animal infection studies.**

604 Mice of the specified age and sex were infected via aerosol exposure using the Glas-Col
605 Inhalation Exposure System (Terre Haute, IN, USA). Fresh cryo-aliquots of *Mtb* H37Rv
606 were used for each infection, diluted in sterile 7H9 broth to empirically determined

607 concentrations to achieve the desired bacterial load on day 1 post-infection. To minimize
608 variability between groups, mice from all experimental groups were infected concurrently
609 and randomly allocated to experimental arms. The bacterial implantation in the lungs was
610 assessed one day after infection by sacrificing 3–5 mice per group and determining
611 colony-forming units (CFUs). Mice were euthanized at specified time points (as outlined
612 in the Results section), and the lungs and spleen were aseptically harvested, weighed
613 and either homogenized by bead-beating for bacterial quantification (Right lung) or stored
614 in 10% neutral-buffered formalin for histopathological analysis (Left lung). CFU
615 enumeration was performed by plating serial dilutions on 7H11 agar supplemented with
616 OADC, followed by incubation at 37°C for 3 to 4 weeks. Bacterial counts were normalized
617 to the weight of the total organ, as previously described[92].

618 **Histopathology to estimate lung inflammation.**

619 For histology, left lungs were fixed by immersion in 10% neutral-buffered formalin (Thermo
620 Fisher Scientific; 5705) for at least 2 days, before it was submitted to the SKCCC
621 Oncology Tissue and Imaging Service Core Laboratory (Johns Hopkins University, School
622 of Medicine) for downstream processing. The lungs were paraffin-embedded, 4 µm-
623 sectioned, and stained with hematoxylin and eosin (H&E). Slides were digitally scanned
624 at 40× using a Hamamatsu Nanozoomer S210 digital slide scanner (Hamamatsu
625 Photonics, Shizuoka, Japan) at 40X magnification (0.23 microns/pixel). Image files were
626 submitted in https://digital.pathology.johnshopkins.edu/ using Concentriq LS platform
627 (Proscia, PA, USA). Lung inflammation was quantified as a percentage of total lung area
628 using an in-house protocol developed with ImageJ software version 1.54m (NIH, USA) to
629 minimize human bias, through standardized software-based settings. Images were first

630 opened in ImageJ, and the scale was set by drawing a line over the scale bar using the
631 line tool and defining the known distance in millimeters under Analyze> Set Scale. Images
632 were then cropped to exclude the ruler (Image > Crop) and saved. For area quantification,
633 the Image> Adjust> Color Threshold tool was used, with consistent settings for hue (0–
634 255), saturation (0–255), and brightness (set based on analysis type)- full lung area=(0-
635 250) and inflamed area= (0-160). After selecting the ROI, the threshold window was
636 closed, and images were converted to binary format using Process> Binary> Make
637 Binary. The Signal to Noise ratio was improved by removing the Outliers- using Process>
638 Noise> Remove Outliers, adjusting the radius (=4) and the Threshold (=50).
639 Measurements were extracted (Analyze> Measure), with the initial setup requiring the
640 selection of "area" and "limit to threshold" under Set Measurements. Processed images
641 were saved, and the steps were repeated for all images with identical parameters to
642 ensure consistency. ROIs were then divided by the total lung area per slide to calculate
643 the ratio of inflamed to lung tissue- area.

644 **Multicolor Flow cytometry to quantify senescent cell population in *Mtb*-infected**
645 **mice lungs and spleen.**

646 To assess markers of senescence (p16+, p21+, and increased SA-βGalactosidase
647 activity) in lung and spleen tissues from *Mtb*-infected mice, organs were harvested at
648 indicated time points and dissociated using the Lung Dissociation Kit (Miltenyi Biotec;130-
649 095-927), and the gentleMACS Octo Dissociator (program m_lung_02), according to the
650 manufacturer's protocol. Single-cell suspensions were obtained by filtering dissociated
651 tissue through 70 µm mesh strainers (Corning; 431751), washing with 5 mL complete
652 RPMI media, and centrifuging at 300g for 5 min at RT. Red blood cells were lysed using

653 ACK lysis buffer (Quality Biological; 118156101), neutralized with complete RPMI, and
654 centrifuged. Cells were stained for viability using a live-dead near-IR dye (1:1000 dilution
655 in PBS; Thermo Fisher Scientific; L10119) and blocked with Rat Anti-Mouse CD16/CD32
656 Fc Block (Clone 2.4G2, BD Pharmingen; 553142). The panel of antibodies to detect the
657 senescent cell population (SenPanel) was designed using FluoroFinder
658 (https://fluorofinder.com/). For extracellular staining, cells were incubated with 50 µL of an
659 antibody cocktail in Brilliant Stain Buffer (BD Biosciences; 563794) containing anti- mouse
660 CD45 (Brilliant Violet 480; BD Biosciences;566095), CD11b (Brilliant Violet 650;
661 BioLegend; 101239), CD45R/B220 (Brilliant Violet 421; BioLegend; 103239), CD3
662 (StarBright Violet 610; BioRad-MCA500SBV610), EpCAM (PerCP-Cy5.5; BioLegend;
663 118220), F4/80 (PE-Dazzle 594; BioLegend; 123145), CD11c (PE-Fire 810; BioLegend;
664 161105), and Siglec-F (Alexa Fluor 700; BioLegend; 155533) for 30 minutes at 4°C in the
665 dark. After extracellular staining, cells were fixed with 4% formaldehyde, washed with
666 PBS, and incubated with the CellEvent™ Senescence Green Flow Cytometry Assay Kit
667 (Thermo Fisher Scientific; C10841; 1:250 dilution) in the senescence reaction buffer for 4
668 hours at 37°C, protected from light and without $CO_2$. Following incubation, cells were
669 washed and permeabilized using Perm/Wash buffer (BD Biosciences; 554723).
670 Intracellular staining was performed by incubating cells with a cocktail containing
671 p14ARF/CDKN2A Antibody (PE; Novus Biologicals; NB200-111PE), p21/CIP1/CDKN1A
672 Antibody (HJ21) (APC; Novus Biologicals; NBP2-47896APC), and CD68 (Brilliant Violet
673 785; BioLegend; 137035) for 60 minutes at 4°C in the dark. After staining, cells were
674 washed, filtered through strainer-capped BD FACS tubes (BD; 352235), and analyzed via
675 flow cytometry. $1\times10^6$ events per sample were acquired using a BD LSR Fortessa™ Cell

676 Analyzer (BD Biosciences), and the data were analyzed with FlowJo software version
677 10.8.1 (BD Biosciences). Single stain controls and compensation matrices were prepared
678 using UltraComp eBeads Plus Compensation Beads (Thermo Fisher Scientific; 01-3333-
679 41) and cells, as required. All flow antibodies were titrated to determine optimal staining
680 concentrations, and only manufacturer-validated antibodies with demonstrated specificity
681 were used. For the analysis, cells were first gated on singlets (FSC-H vs. FSC-A) and live
682 cells (live-dead near-IR negative) before further selection of cell types. T cells are
683 CD45+CD3+ and B cells are CD45+B220+. Myeloid cells: Tissue-resident Macrophages
684 are CD45+CD68+F4/80+CD11B-CD11C+, Interstitial macrophages are CD45+CD68+
685 F4/80+CD11B+CD11C+SiglecF-, Monocytes are CD45+CD68+F4/80+CD11B+CD11C-,
686 and Dendritic cells are CD45+CD68+F4/80-CD11B+CD11C+. Gating for $p16^+$, $p21^+$, and
687 SA-$\beta Gal^+$ events for each cell type were established using reference cells from *Mtb*-
688 infected WT B6 mice (set at 1 %).

689 **Immunohistochemistry against p21 and γH2A.X (phosphor S139) in mice lungs.**

690 Immunostaining was conducted at the SKCCC Oncology Tissue and Imaging Service
691 Core Laboratory, Johns Hopkins University, School of Medicine. Immunolabeling for
692 γH2A.X (phospho S139) and p21 was performed on 4 µm-thick formalin-fixed, paraffin-
693 embedded (FFPE) tissue sections using the Ventana Discovery Ultra autostainer (Roche
694 Diagnostics). Sections underwent onboard dewaxing and rehydration, followed by
695 epitope retrieval in Ventana Ultra CC1 buffer (Roche Diagnostics; 6414575001) at 96°C
696 for 64 minutes. Primary antibodies- anti-gamma H2A.X (phospho S139) [EP854(2)Y]
697 (Abcam; ab81299; 1:1000 dilution) and Recombinant Anti-p21 antibody [EPR18021]
698 (Abcam; ab188224; 1:1000 dilution) were applied as indicated, at 36°C for 60 minutes.

699 Detection of the primary antibodies was achieved using the anti-rabbit HQ detection
700 system (Roche Diagnostics; Catalog 7017936001 and 7017812001), followed by
701 visualization with the Chromomap DAB IHC detection kit (Roche Diagnostics;
702 5266645001). Sections were counterstained with Mayer's hematoxylin, dehydrated, and
703 mounted. Whole-slide imaging was performed at the Oncology Tissue Services Core of
704 Johns Hopkins University using a Hamamatsu Nanozoomer S210 digital slide scanner
705 (Hamamatsu Photonics, Shizuoka, Japan) at 40X magnification (0.23 microns/pixel).
706 Images were visualized using the Concentriq digital pathology platform (Proscia,
707 Philadelphia, PA) and analyzed in ImageJ following a previously established in- house
708 protocol. Area quantification was performed using the Image> Adjust> Color Threshold
709 tool in ImageJ, applying consistent hue (0–255), saturation (0–255), and brightness
710 thresholds based on analysis type: full lung area (0–250) and DAB+ area (0–120).
711 Identical thresholds and detection settings were applied for all slides to ensure
712 consistency across analyses.

713 **Senescence-associated secretory phenotype (SASP)- cytokine quantification in**
714 ***Mtb*- infected mice lungs.**

715 To estimate SASP- cytokine levels, lung homogenates were centrifuged at 14,000 RPM
716 for 10 minutes at 4°C, and the resulting supernatants were filtered by a 0.2 µm filter, prior
717 to removal from the BSL3 facility. Supernatants were flash-frozen in liquid nitrogen and
718 stored at –80°C until cytokine quantification analysis. Cytokine levels in the lung
719 homogenate were measured using the LEGENDplex Mouse Inflammation Panel 13-plex
720 kit (BioLegend; 740446) following the manufacturer's protocol. Data acquisition was
721 performed on the CytoFLEX Flow Cytometer (Beckman Coulter), and cytokine

722 concentrations were analyzed using the LEGENDplex data analysis software Suite
723 (BioLegend). The amount of SASP cytokines were normalized to the protein
724 concentration of the homogenate (as measured by the BCA Assay kit).

725 **Drug preparation and study arms to test Senolytics as host- directed therapy *in***
726 ***vivo*.**

727 Dasatinib (Cayman Chemical; 11498), Fisetin (Cayman Chemical;15246), and Quercetin
728 (Millipore Sigma; Q4951) at required concentrations were first dissolved in 10ml DMSO
729 (Millipore Sigma; D2650) to make a stock solution. This mixture was then added to 190
730 ml of the Vehicle (60% Phosal 50 PG (Lipoid LLC; 368315), 30% PEG 400 (Sigma Aldrich;
731 202398), and 10% Ethanol) to prepare the final Senolytics reagent. Ethambutol (Millipore
732 Sigma; E4630) and Rifampicin (Millipore Sigma; R3501) were used as anti-*Mtb* drug
733 control. Solutions of Ethambutol and Rifampicin in distilled water were prepared and
734 stored at 4 °C.

735 After the day of aerosol infection, female mice were randomly divided into 4 groups (n = 4-
736 8 per group, as indicated in the Results). Feed and water were given *ad libitum*. Treatment
737 with drugs started at 2 weeks (*B6.Sst1S* mice and WT B6 Old), or 4 weeks (for WT B6
738 mice) post-infection. The drug treatment continued for another 6 weeks (for *B6.Sst1S*
739 mice), 3 weeks (for WT B6 Old) or 4 weeks (for WT B6). Treated mice were administered
740 Ethambutol (100 mg/kg of body weight) by oral gavage, once daily, 5 times a week.
741 Vehicle or Senolytics (Dasatinib: 5 mg/kg, Fisetin: 100 mg/kg, and Quercetin: 50 mg/kg
742 of body weight of mice) were administered by oral gavage, once daily, 3 times a week.
743 The fourth group received both the Ethambutol and Senolytics combination. All drugs
744 were administered in a total volume of 0.2 ml per treatment. Three infected mice were

745 sacrificed at the start of treatment as pretreatment controls. At indicated time points, mice
746 were sacrificed, and the lungs and spleen were harvested for the measurement of
747 bacterial burden, IHC, FACS and histopathology.

748 **Time to death assay.**

749 To examine if the Senolytics administration can improve the survival and body weight, the
750 survival of both male and female *B6.Sst1S* mice (8-10 weeks old) following *Mtb* infection
751 were assessed. Mice were infected via the aerosol route using a Glas-Col aerosolization
752 instrument to deliver a high dose of *Mtb* to the *B6.Sst1S* lungs (approximately 100 CFU).
753 After 3 weeks post-infection, infected mice were randomly divided into 4 groups and the
754 drug was administered as mentioned above, with slight modifications. The drug treatment
755 continued for another 4 weeks, where mice were administered Ethambutol (50 mg/kg of
756 body weight) by oral gavage, once daily, 5 times a week. In the second week, Ethambutol
757 (50 mg/kg of body weight) was combined with Rifampicin (10 mg/kg of body weight) for 1
758 week. Vehicle or Senolytics (Dasatinib: 5 mg/kg, Fisetin: 100 mg/kg, and Quercetin: 50
759 mg/kg of body weight of mice) were administered by oral gavage, once daily, 3 times a
760 week. The fourth group received both the Ethambutol and Senolytics combination. All
761 drugs were administered in a total volume of 0.2 ml per treatment. All mice were monitored
762 daily for signs of disease progression, including weight loss, lethargy, hunched posture,
763 and reduced activity. Survival data were analyzed using Kaplan-Meier survival curves to
764 determine the median time to death and assess differences between treatment groups.

765 **Statistical analysis.**

766 Statistical analyses were performed using GraphPad Prism version 10.4.0 software.
767 Normality distribution was first assessed using the Shapiro-Wilk test. For comparisons of
768 lung CFUs, data was $\log_{10}$-transformed and checked for normality before the analysis.
769 Statistical significance was determined using unpaired two-tailed Student's t-tests or
770 Mann Whitney test for two-group comparisons, and one-way or two- way ANOVA with
771 post hoc tests for multiple- group comparisons. Kaplan-Meier survival analysis was
772 conducted for time-to-death (TTD) studies, with group differences assessed by the Log-
773 rank (Mantel-Cox) test. In animal experiments, each data point represented a single
774 mouse, and experiments were randomized, though blinding was not implemented.
775 Results are presented as mean ± SEM, with error bars indicating SEM. *p*-values less than
776 0.05 were considered statistically significant.

777 **Contact for reagent and resource sharing.**

778 All data associated with this study are present in the paper- either in the Results section
779 or in the Supplementary files. Requests for further details on resources, protocol, and
780 reagents can be directed to the corresponding author- Prof. William R Bishai. Raw data
781 generated during this study is provided as a separate Excel file labeled "Source Data file".
782 The RNA sequencing and Spatial transcriptomics datasets are available on NCBI's Gene
783 Expression Omnibus (GEO). The *B6.Sst1S* mice used in this study are available for
784 academic and non-commercial research upon request to Prof. Igor Kramnik, under a
785 Material Transfer Agreement.

786

787

## Acknowledgements

We gratefully acknowledge the support of the NIH grants AI152688, AI155602, CA006973, and R01HL126066 (to IK). We extend our gratitude to the SKCCC Core centers for their assistance with Histology and Flow cytometry. The funders have no role in study-design, data collection and interpretation, and the decision to submit the work for publication or preparation of the manuscript. We sincerely thank all the members of Prof. Bishai lab and Prof. Kramnik lab, for their valuable suggestions and discussions throughout this project. The schematic figures in this study were created using BioRender (with Academic Lab License).

## Author contributions.

Funding Acquisition was contributed by- WB, IK. Conceptualization- WB, IK, SS. Methodology- WB, IK, SS, YMM, BK, SY, LK. Investigation and Formal Analysis- WB, IK, SS. Data curation and Validation- SS, SY, LK. Writing original draft- WB, IK, SS, SY. Review and editing manuscript- WB, IK, SS, YMM, BK, SY, LK.

## Conflict of interest statement.

The authors declare that they have no competing or conflicting interests.

## References


1. *2024 Global Tuberculosis Report*. https://www.who.int/teams/global-tuberculosis-programme/tb-reports/global-tuberculosis-report-2024.

2. Horton, K. C., Richards, A. S., Emery, J. C., Esmail, H. & Houben, R. M. G. J. Reevaluating progression and pathways following Mycobacterium tuberculosis infection within the spectrum of tuberculosis. *Proc Natl Acad Sci U S A* **120**, e2221186120 (2023).

3. Sossen, B. *et al.* The natural history of untreated pulmonary tuberculosis in adults: a systematic review and meta-analysis. *Lancet Respir Med* **11**, 367–379 (2023).

4. Richards, A. S. *et al.* Quantifying progression and regression across the spectrum of pulmonary tuberculosis: a data synthesis study. *Lancet Glob Health* **11**, e684–e692 (2023).

5. Nguyen, H. V., Tiemersma, E., Nguyen, N. V., Nguyen, H. B. & Cobelens, F. Disease Transmission by Patients With Subclinical Tuberculosis. *Clin Infect Dis* **76**, 2000–2006 (2023).

6. Chen, R. Y. *et al.* Radiological and functional evidence of the bronchial spread of tuberculosis: an observational analysis. *Lancet Microbe* **2**, e518–e526 (2021).

7. GBD Tuberculosis Collaborators. The global burden of tuberculosis: results from the Global Burden of Disease Study 2015. *Lancet Infect Dis* **18**, 261–284 (2018).

8. Olmo-Fontánez, A. M. & Turner, J. Tuberculosis in an Aging World. *Pathogens* **11**, (2022).

9. Negin, J., Abimbola, S. & Marais, B. J. Tuberculosis among older adults--time to take notice. *Int J Infect Dis* **32**, 135–7 (2015).

10. Caraux-Paz, P., Diamantis, S., de Wazières, B. & Gallien, S. Tuberculosis in the Elderly. *J Clin Med* **10**, 5888 (2021).

11. Teo, A. K. J. *et al.* Tuberculosis in older adults: challenges and best practices in the Western Pacific Region. *Lancet Reg Health West Pac* **36**, 100770 (2023).

12. Orme, I. M. Aging and immunity to tuberculosis: prolonged survival of old mice infected with Mycobacterium tuberculosis by adoptive immunization with memory-immune T lymphocytes. *Cell Immunol* **118**, 229–33 (1989).

13. Orme, I. M. A mouse model of the recrudescence of latent tuberculosis in the elderly. *Am Rev Respir Dis* **137**, 716–8 (1988).

14. Turner, J., Frank, A. A. & Orme, I. M. Old mice express a transient early resistance to pulmonary tuberculosis that is mediated by CD8 T cells. *Infect Immun* **70**, 4628–37 (2002).

844 15. Torrelles, J. B. *et al.* The Impact of Aging on the Lung Alveolar Environment,
845 Predetermining Susceptibility to Respiratory Infections. *Frontiers in Aging* **3**, 1–9
846 (2022).

847 16. Canan, C. H. *et al.* Characterization of lung inflammation and its impact on
848 macrophage function in aging. *J Leukoc Biol* **96**, 473–480 (2014).

849 17. Lafuse, W. P. *et al.* Identification of an Increased Alveolar Macrophage
850 Subpopulation in Old Mice That Displays Unique Inflammatory Characteristics and
851 Is Permissive to Mycobacterium tuberculosis Infection. *J Immunol* **203**, 2252–
852 2264 (2019).

853 18. Olmo-Fontánez, A. M. *et al.* Impact of the elderly lung mucosa on Mycobacterium
854 tuberculosis transcriptional adaptation during infection of alveolar epithelial cells.
855 *Microbiol Spectr* **12**, e0179024 (2024).

856 19. Olmo-Fontánez, A. M. *et al.* Human alveolar lining fluid from the elderly promotes
857 Mycobacterium tuberculosis intracellular growth and translocation into the cytosol
858 of alveolar epithelial cells. *Mucosal Immunol* **17**, 155–168 (2024).

859 20. Moliva, J. I. *et al.* The Lung Mucosa Environment in the Elderly Increases Host
860 Susceptibility to Mycobacterium tuberculosis Infection. *Journal of Infectious*
861 *Diseases* **220**, 514–523 (2019).

862 21. Di Micco, R., Krizhanovsky, V., Baker, D. & d'Adda di Fagagna, F. Cellular
863 senescence in ageing: from mechanisms to therapeutic opportunities. *Nat Rev*
864 *Mol Cell Biol* **22**, 75–95 (2021).

865 22. Wissler Gerdes, E. O., Zhu, Y., Tchkonia, T. & Kirkland, J. L. Discovery,
866 development, and future application of senolytics: theories and predictions. *FEBS*
867 *J* **287**, 2418–2427 (2020).

868 23. Kennedy, B. K. *et al.* Geroscience: linking aging to chronic disease. *Cell* **159**,
869 709–13 (2014).

870 24. Wang, B., Han, J., Elisseeff, J. H. & Demaria, M. The senescence-associated
871 secretory phenotype and its physiological and pathological implications. *Nat Rev*
872 *Mol Cell Biol* **25**, 958–978 (2024).

873 25. Xu, M. *et al.* Transplanted Senescent Cells Induce an Osteoarthritis-Like
874 Condition in Mice. *J Gerontol A Biol Sci Med Sci* **72**, 780–785 (2017).

875 26. Franco, A. C. *et al.* Senescent cell transplantation into the skin induces age-
876 related peripheral dysfunction and cognitive decline. *Aging Cell* **24**, (2025).

877 27. Childs, B. G., Durik, M., Baker, D. J. & van Deursen, J. M. Cellular senescence in
878 aging and age-related disease: from mechanisms to therapy. *Nat Med* **21**, 1424–
879 35 (2015).

880 28. Justice, J. N. *et al.* Senolytics in idiopathic pulmonary fibrosis: Results from a first-
881 in-human, open-label, pilot study. *EBioMedicine* **40**, 554–563 (2019).

882 29. Pichugin, A. V., Yan, B. S., Sloutsky, A., Kobzik, L. & Kramnik, I. Dominant role of
883 the sst1 locus in pathogenesis of necrotizing lung granulomas during chronic
884 tuberculosis infection and reactivation in genetically resistant hosts. *American*
885 *Journal of Pathology* **174**, 2190–2201 (2009).

886 30. Yan, B. S., Kirby, A., Shebzukhov, Y. V., Daly, M. J. & Kramnik, I. Genetic
887 architecture of tuberculosis resistance in a mouse model of infection. *Genes*
888 *Immun* **7**, 201–210 (2006).

889 31. Ji, D. X. *et al.* Type I interferon-driven susceptibility to Mycobacterium tuberculosis
890 is mediated by IL-1Ra. *Nat Microbiol* **4**, 2128–2135 (2019).

891 32. Yabaji, S. M. *et al.* Cell state transition analysis identifies interventions that
892 improve control of Mycobacterium tuberculosis infection by susceptible
893 macrophages. *Sci Adv* **9**, eadh4119 (2023).

894 33. Pan, H. *et al.* Ipr1 gene mediates innate immunity to tuberculosis. *Nature* **434**,
895 767–772 (2005).

896 34. Krug, S. *et al.* Adjunctive Integrated Stress Response Inhibition Accelerates
897 Tuberculosis Clearance in Mice. *mBio* **14**, e0349622 (2023).

898 35. Bhattacharya, B. *et al.* The integrated stress response mediates necrosis in
899 murine Mycobacterium tuberculosis granulomas. *Journal of Clinical Investigation*
900 **131**, (2021).

901 36. Fraschilla, I., Amatullah, H., Rahman, R. U. & Jeffrey, K. L. Immune chromatin
902 reader SP140 regulates microbiota and risk for inflammatory bowel disease. *Cell*
903 *Host Microbe* **30**, 1370-1381.e5 (2022).

904 37. Ji, D. X. *et al.* Role of the transcriptional regulator SP140 in resistance to bacterial
905 infections via repression of type I interferons. *Elife* **10**, (2021).

906 38. Yabaji, S. M. *et al.* Lipid Peroxidation and Type I Interferon Coupling Fuels
907 Pathogenic Macrophage Activation Causing Tuberculosis Susceptibility. *bioRxiv*
908 (2024) doi:10.1101/2024.03.05.583602.

909 39. Moreira-Teixeira, L. *et al.* Type I IFN exacerbates disease in tuberculosis-
910 susceptible mice by inducing neutrophil-mediated lung inflammation and NETosis.
911 *Nat Commun* **11**, 5566 (2020).

912 40. Berry, M. P. R. *et al.* An interferon-inducible neutrophil-driven blood transcriptional
913 signature in human tuberculosis. *Nature* **466**, 973–7 (2010).

914 41. Kotov, D. I. *et al.* Early cellular mechanisms of type I interferon-driven
915 susceptibility to tuberculosis. *Cell* **186**, 5536-5553.e22 (2023).

916 42. Kalinin, A., Zubkova, E. & Menshikov, M. Integrated Stress Response (ISR)
917 Pathway: Unraveling Its Role in Cellular Senescence. *Int J Mol Sci* **24**, (2023).

918 43. Payea, M. J. *et al.* Senescence suppresses the integrated stress response and
919 activates a stress-remodeled secretory phenotype. *Mol Cell* **84**, 4454-4469.e7
920 (2024).

921 44. Zhou, Y. *et al.* Metascape provides a biologist-oriented resource for the analysis of
922 systems-level datasets. *Nat Commun* **10**, 1523 (2019).

923 45. Saul, D. *et al.* A new gene set identifies senescent cells and predicts senescence-
924 associated pathways across tissues. *Nat Commun* **13**, (2022).

925 46. Sharpless, N. E. & Sherr, C. J. Forging a signature of in vivo senescence. *Nat*
926 *Rev Cancer* **15**, 397–408 (2015).

927 47. González-Gualda, E., Baker, A. G., Fruk, L. & Muñoz-Espín, D. A guide to
928 assessing cellular senescence in vitro and in vivo. *FEBS Journal* **288**, 56–80
929 (2021).

930 48. Suda, M. *et al.* Senolytic vaccination improves normal and pathological age-
931 related phenotypes and increases lifespan in progeroid mice. *Nat Aging* **1**, 1117–
932 1126 (2021).

933 49. Zhu, Y. *et al.* The Achilles' heel of senescent cells: from transcriptome to senolytic
934 drugs. *Aging Cell* **14**, 644–58 (2015).

935 50. Zhang, L. *et al.* Cellular senescence: a key therapeutic target in aging and
936 diseases. *J Clin Invest* **132**, (2022).

937 51. Raffaele, M. & Vinciguerra, M. The costs and benefits of senotherapeutics for
938 human health. *Lancet Healthy Longev* **3**, e67–e77 (2022).

939 52. Robbins, P. D. *et al.* Senolytic Drugs: Reducing Senescent Cell Viability to Extend
940 Health Span. *Annu Rev Pharmacol Toxicol* **61**, 779–803 (2021).

941 53. Chaib, S., Tchkonia, T. & Kirkland, J. L. Cellular senescence and senolytics: the
942 path to the clinic. *Nat Med* **28**, 1556–1568 (2022).

943 54. Lee, E. *et al.* Exploring the effects of Dasatinib, Quercetin, and Fisetin on DNA
944 methylation clocks: a longitudinal study on senolytic interventions. *Aging* **16**,
945 3088–3106 (2024).

946 55. Shah, N. P. *et al.* Overriding imatinib resistance with a novel ABL kinase inhibitor.
947 *Science* **305**, 399–401 (2004).

948 56. Yousefzadeh, M. J. *et al.* Fisetin is a senotherapeutic that extends health and
949 lifespan. *EBioMedicine* **36**, 18–28 (2018).

950 57. Zhu, Y. *et al.* New agents that target senescent cells: the flavone, fisetin, and the
951 BCL-XL inhibitors, A1331852 and A1155463. *Aging* **9**, 955–963 (2017).

952 58. Lim, J. Y., Lee, J. Y., Byun, B. J. & Kim, S. H. Fisetin targets phosphatidylinositol-
953 3-kinase and induces apoptosis of human B lymphoma Raji cells. *Toxicol Rep* **2**,
954 984–989 (2015).

955 59. Kim, J. A. *et al.* Fisetin, a dietary flavonoid, induces apoptosis of cancer cells by
956 inhibiting HSF1 activity through blocking its binding to the hsp70 promoter.
957 *Carcinogenesis* **36**, 696–706 (2015).

958 60. Amaral, E. P. *et al.* BACH1 promotes tissue necrosis and Mycobacterium
959 tuberculosis susceptibility. *Nat Microbiol* **9**, 120–135 (2024).

960 61. Orme, I. Mechanisms underlying the increased susceptibility of aged mice to
961 tuberculosis. *Nutr Rev* **53**, S35-8; discussion S38-40 (1995).

962 62. Vesosky, B. & Turner, J. The influence of age on immunity to infection with
963 Mycobacterium tuberculosis. *Immunol Rev* **205**, 229–43 (2005).

964 63. Rottinghaus, E. K., Vesosky, B. & Turner, J. TLR-2 independent recognition of
965 Mycobacterium tuberculosis by CD11c+ pulmonary cells from old mice. *Mech*
966 *Ageing Dev* **131**, 405–14 (2010).

967 64. Bobak, C. A. *et al.* Increased DNA methylation, cellular senescence and
968 premature epigenetic aging in guinea pigs and humans with tuberculosis. *Aging*
969 **14**, 2174–2193 (2022).

970 65. DiNardo, A. R. *et al.* DNA hypermethylation during tuberculosis dampens host
971 immune responsiveness. *J Clin Invest* **130**, 3113–3123 (2020).

972 66. Udomsinprasert, W. *et al.* Leukocyte telomere length as a diagnostic biomarker
973 for anti-tuberculosis drug-induced liver injury. *Sci Rep* **10**, (2020).

974 67. Freimane, L. *et al.* Telomere length and mitochondrial DNA copy number in
975 multidrug-resistant tuberculosis. *Tuberculosis* **131**, (2021).

976 68. Katoto, P. D. M. C. *et al.* Telomere length and outcome of treatment for pulmonary
977 tuberculosis in a gold mining community. *Sci Rep* **11**, (2021).

978 69. Lochab, S., Singh, Y., Sengupta, S. & Nandicoori, V. K. Mycobacterium
979 tuberculosis exploits host ATM kinase for survival advantage through secA2
980 secretome. *Elife* **9**, (2020).

981 70. Cumming, B. M., Addicott, K. W., Adamson, J. H. & Steyn, A. J. C. Mycobacterium
982 tuberculosis induces decelerated bioenergetic metabolism in human
983 macrophages. *Elife* **7**, 1–28 (2018).

984 71. Cumming, B. M. *et al.* Mycobacterium tuberculosis arrests host cycle at the G1/S
985 transition to establish long term infection. *PLoS Pathog* **13**, (2017).

986 72. Cyktor, J. C. *et al.* Killer cell lectin-like receptor G1 deficiency significantly
987 enhances survival after Mycobacterium tuberculosis infection. *Infect Immun* **81**,
988 1090–9 (2013).

989 73. Chang, E., Cavallo, K. & Behar, S. M. CD4 T cell dysfunction is associated with
990 bacterial recrudescence during chronic tuberculosis. *Nat Commun* **16**, 2636
991 (2025).

992 74. Chien, Y. *et al.* Control of the senescence-associated secretory phenotype by NF-
993 κB promotes senescence and enhances chemosensitivity. *Genes Dev* **25**, 2125–
994 36 (2011).

995 75. Miwa, S., Kashyap, S., Chini, E. & von Zglinicki, T. Mitochondrial dysfunction in
996 cell senescence and aging. *J Clin Invest* **132**, (2022).

997 76. VanValkenburg, A. *et al.* Malnutrition leads to increased inflammation and
998 expression of tuberculosis risk signatures in recently exposed household contacts
999 of pulmonary tuberculosis. *Front Immunol* **13**, 1011166 (2022).

1000 77. Cottage, C. T. *et al.* Targeting p16-induced senescence prevents cigarette smoke-
1001 induced emphysema by promoting IGF1/Akt1 signaling in mice. *Commun Biol* **2**,
1002 307 (2019).

1003 78. Marino, F. *et al.* Diabetes-Induced Cellular Senescence and Senescence-
1004 Associated Secretory Phenotype Impair Cardiac Regeneration and Function
1005 Independently of Age. *Diabetes* **71**, 1081–1098 (2022).

1006 79. Topiwala, A. *et al.* Alcohol consumption and telomere length: Mendelian
1007 randomization clarifies alcohol's effects. *Mol Psychiatry* **27**, 4001–4008 (2022).

1008 80. Restrepo, B. I. *et al.* Differential Role of Type 2 Diabetes as a Risk Factor for
1009 Tuberculosis in the Elderly versus Younger Adults. *Pathogens* **11**, 1551 (2022).

1010 81. Auld, E. *et al.* HIV Infection Is Associated with Shortened Telomere Length in
1011 Ugandans with Suspected Tuberculosis. *PLoS One* **11**, e0163153 (2016).

1012 82. Auld, S. C. *et al.* Pathogenesis of Post-Tuberculosis Lung Disease: Defining
1013 Knowledge Gaps and Research Priorities at the Second International Post-
1014 Tuberculosis Symposium. *Am J Respir Crit Care Med* **210**, 979–993 (2024).

1015 83. Ravimohan, S., Kornfeld, H., Weissman, D. & Bisson, G. P. Tuberculosis and lung
1016 damage: from epidemiology to pathophysiology. *Eur Respir Rev* **27**, (2018).

1017 84. Auld, S. C. *et al.* Pulmonary restriction predicts long-term pulmonary impairment
1018 in people with HIV and tuberculosis. *BMC Pulm Med* **21**, 19 (2021).

1019 85. Allwood, B. W. *et al.* Perspectives from the 2nd International Post-Tuberculosis
1020 Symposium: mobilising advocacy and research for improved outcomes. *IJTLD
1021 open* **1**, 111–123 (2024).

1022 86. Schafer, M. J. *et al.* Cellular senescence mediates fibrotic pulmonary disease. *Nat*
1023 *Commun* **8**, 14532 (2017).

1024 87. Parveen, S. *et al.* Glutamine metabolism inhibition has dual immunomodulatory
1025 and antibacterial activities against Mycobacterium tuberculosis. *Nat Commun* **14**,
1026 7427 (2023).

1027 88. Love, M. I., Huber, W. & Anders, S. Moderated estimation of fold change and
1028 dispersion for RNA-seq data with DESeq2. *Genome Biol* **15**, 1–21 (2014).

1029 89. Shee, S. *et al.* Moxifloxacin-Mediated Killing of Mycobacterium tuberculosis
1030 Involves Respiratory Downshift, Reductive Stress, and Accumulation of Reactive
1031 Oxygen Species. *Antimicrob Agents Chemother* **66**, (2022).

1032 90. Merritt, C. R. *et al.* Multiplex digital spatial profiling of proteins and RNA in fixed
1033 tissue. *Nat Biotechnol* **38**, 586–599 (2020).

1034 91. Danaher, P. *et al.* Advances in mixed cell deconvolution enable quantification of
1035 cell types in spatial transcriptomic data. *Nat Commun* **13**, 385 (2022).

1036 92. Krug, S. *et al.* Inhibition of host PARP1 contributes to the anti-inflammatory and
1037 antitubercular activity of pyrazinamide. *Nat Commun* **14**, 8161 (2023).

1038

1039

1040 **Figure legends.**

1041 **Fig. 1. Evidence of senescence-like phenotype in BMDMs derived from young *B6.***
1042 ***Sst1S* and aged WT B6 mice. (a)** Schematic to determine senescence associated
1043 markers in BMDMs. **(b)** BMDMs were infected for 4 hours with *Mtb* H37Rv at MOI=10,
1044 followed by removal of extracellular bacteria by extensive washing with warm media.
1045 Intramacrophage survival was determined by enumerating CFU at 2 days post-infection.
1046 The data are means ± SEM of two independent experiments (n=4). **(c)** Median
1047 Fluorescence intensity of fluorescent SA-βGal substrate by live BMDMs in presence or
1048 absence of TNFα for 48 h. 10 μM Etoposide treated WT B6 BMDMs or BMDMs from aged
1049 WT B6 mice are used as positive control. **(d)** Representative images of SA-βGal- positive
1050 BMDMs (PFA-fixed) located at the center of the TC-treated well at 20X magnification by
1051 bright field microscopy. **(e)** mRNA levels of SASP-associated genes normalized to *ActB*
1052 are shown as determined by qPCR. **(f)** BrdU incorporation by BMDMs in absence or
1053 presence of TNFα, respectively with time. The data are means ± SEM. Data is
1054 representative of two independent experiments. ($p$>0.05: non- significant (ns), $p$<0.05: *,
1055 $p$<0.01: **, $p$<0.001: ***, $p$<0.0001: ***, one-way ANOVA with Tukey's (b, c, f) or Sidak's
1056 (e) multiple comparisons test).

1057 **Fig. 2. Detection of Senescence- associated markers during early stages of disease**
1058 **progression in *Mtb* infected mice. (a)** Schematics of Spatial transcriptomics using a
1059 Nanostring GeoMX Digital Spatial Profiler to determine differential gene expression in
1060 cells at non-controlling multibacillary granulomatous lesions (NC) relative to controlling
1061 lesions (C) in *B6.Sst1S* mice lungs. (n= 8 region of interests (ROI) from 2 mice). **(b)**
1062 Volcano plot to show differentially expressed genes between controlling and non-

1063 controlling granulomatous lesions. Significantly upregulated (fold change> 2) and
1064 downregulated (fold change< 2) genes (*p.adj*< 0.05) in NC relative to C granulomas are
1065 shown in red and cyan, respectively. Top senescence associated genes in upregulated-
1066 DEGs are labelled. **(c)** Schematics of the experimental strategy to measure senescence
1067 markers *in vivo* at 2- and 4-weeks post infection (p.i.). Day1 CFU=39. *Mtb* H37Rv burden
1068 at indicated time points in WT B6, *B6.Sst1S* and WT B6 old mice **(d)** lungs and **(e)** spleen.
1069 The data are means ± SEM. Each data point represents a mouse. *p* was determined by
1070 two-way ANOVA with Tukey's multiple comparisons test. Representative H&E-stained
1071 and Immunohistochemistry against γH2A.X and p21 of mice lungs at **(f)** 2 weeks p.i. and
1072 **(g)** 4 weeks p.i. **(h)** ImageJ quantification of lung pathology (% inflamed area) in
1073 uninfected mice and *Mtb* H37Rv infected mice lungs at 2 weeks and 4 weeks p.i. (n=4-
1074 6). Squares indicate necrotic granulomas. **(i)** ImageJ quantification of γH2A.X-stained
1075 area in uninfected mice and *Mtb* H37Rv infected mice lungs at 2 weeks and 4 weeks p.i.
1076 (n=4-6). The data are means ± SEM. Each data point represents a mouse. *p* values are
1077 indicated as determined by statistical analysis between two groups as measured by
1078 unpaired two- tailed Student's t test (normal distribution) or Mann Whitney test.

1079 **Fig. 3. Detection of senescent cell population and SASP cytokines by flow**
1080 **cytometry during early stages of disease progression in *Mtb* infected mice. (a)**
1081 Schematics of the experimental strategy to measure senescence markers (p21, p16 and
1082 SA- βGal activity) and SASP cytokines levels in mice lungs at 10 and 20 days p.i. Day 1
1083 CFU= 55. **(b)** %p21+p16+ and **(c)** %SA-βGal+ (CellEvent Senescence green+) cells out
1084 of all live lung (uninfected and *Mtb*-infected mice) and Spleen (*Mtb*-infected mice) cells at
1085 10 days p.i. as determined by multicolor flow cytometry. **(d)** %p21+p16+ and **(e)** %SA-

1086 βGal+ cells out of different lung- cell types at 10 days p.i., as determined by multicolor
1087 flow cytometry. Gating for $p16^+$, $p21^+$, and SA-$\beta Gal^+$ events for each cell type were
1088 established using reference cells from *Mtb*-infected WT B6 mice (set at 1 %). (AMs:
1089 Alveolar macrophages, IMs: Interstitial macrophages) **(f)** Normalized concentration of
1090 SASP- cytokines in lung homogenates at 20 dpi and 4 wpi as measured by a
1091 LEGENDplex™ Mouse Inflammation Panel (13-plex). The data are means ± SEM. Each
1092 data point represents a mouse (n=11-12). (two-way ANOVA with Tukey's (b- e) or
1093 Dunnett's (f) multiple comparisons test).

1094 **Fig. 4. Global transcriptomics data by bulk-RNA Sequencing revealed upregulation**
1095 **of pro-survival pathways- PI3K-ERK1/2 and MAPK cascade in BMDMs derived from**
1096 **young *B6.Sst1S* relative to young WTB6 BMDMs, after treatment with TNFα and**
1097 ***Mtb* infection. (a)** Schematic of the experiment. **(b)** Selective representation of Gene-
1098 Ontology (GO) analysis for the differentially expressed genes (= 1177) indicating all
1099 enriched (*p.adj*< 0.05) signaling pathways. The size of the bubble indicates the
1100 percentage of DEGs out of total genes in that GO class and color indicates number of
1101 DEGs in the respective GO class. **(c)** Volcano plot of DEGs with upregulated genes in
1102 stressed (TNFα- treated and *Mtb*- infected) *B6.Sst1S* BMDMs ($log_2$ fold change >1; *p.*
1103 *adj.*< 0.05) shown in light gray and downregulated genes ($log_2$ fold change <1; *p. adj.*<
1104 0.05) shown in light pink, relative to stressed WT B6 BMDMs. Genes representative of
1105 top significantly enriched GO class- Receptor tyrosine kinase signaling/ PI3K pathway
1106 (shown in orange), MAPK cascade (blue), anti-apoptotic genes (red) and SenMayo gene
1107 set (pink) are shown. Top expected downregulated genes- *Sp140* and *Sp110* are shown
1108 in yellow.

1109 **Fig. 5. Senolytics DQF administration with or without anti-TB drug improved**
1110 **survival, body weight and reduced *Mtb* burden in mice. (a)** Both male and female
1111 *B6.Sst1S* mice were aerosol infected with 91 CFU of *Mtb* H37Rv and at 3 weeks p.i., mice
1112 were oral gavaged with vehicle (n=16 mice) or indicated drug regimens (n=11 mice) for
1113 the next 4 weeks. Mice were monitored for changes in body weight and survival after the
1114 start of drug treatment. **(a)** Kaplan-Meir survival curve of *B6.Sst1S* mice given varying
1115 drug regimens. Line indicates duration of oral gavage therapy. Indicated *p* values are
1116 measured by log-rank (Mantel-Cox) test. **(b)** Changes in body weight are plotted as a %
1117 change in body weight of surviving mice relative to Day 1 p.i. over time. The data are
1118 means ± SEM. ($p<0.05$: *, two-way ANOVA with Tukey's multiple comparisons test). **(c)**
1119 The experimental strategy. Day 1 CFU in *B6.Sst1S* mice= 11; WT B6 young and old mice=
1120 126. *Mtb* H37Rv burden in **(d)** lung and **(e)** spleen of *B6.Sst1S* (left), old WT B6 mice
1121 (center), and WT B6 (right), at indicated time points (n=4-7). Square indicates CFU below
1122 the limit of detection (=10). The green arrow indicates the start of drug treatment. The
1123 data are means ± SEM. Statistical analysis between two groups was done by unpaired
1124 two- tailed Student's t test.

1125 **Fig. 6. Senolytics administration alone, and in combination with ethambutol**
1126 **reduced lung pathology and senescence-associated markers in *Mtb* H37Rv**
1127 **infected *B6.Sst1S* and WT B6 old mice. (a)** Representative H&E-stained images of *Mtb*-
1128 infected mice lungs treated with Vehicle or drugs, and respective ImageJ-based
1129 quantification. Yellow arrow indicates necrotic granuloma in Vehicle treated *B6.Sst1S*
1130 mice at 5 wpi. The data are means ± SEM. Each data point represents a mouse. Statistical
1131 analysis between two groups was done by unpaired two- tailed Student's t test. Square

1132 represents necrotic granuloma formation in the lung. **(b)** Representative γH2A.X-
1133 Immunohistochemistry images of mice after lungs vehicle/ drugs treatment, and
1134 respective Violin plots to show ImageJ quantification of γH2A.X-stained area. Each data
1135 point represents a mouse. Statistical analysis between two groups was done by unpaired
1136 two- tailed Student's t test. **(c)** %p21+βGal+ and %p16+βGal+ subpopulation observed
1137 in all live lung cells of *Mtb*-infected mice (n= 5-8). The data are means ± SEM. Each data
1138 point represents a mouse. Statistical analysis was calculated by two-way ANOVA with
1139 Dunnett's multiple comparisons test.

1140 Bubble plot to show %p21+βGal+ and %p16+βGal+ subpopulation in different lung cell
1141 types in *Mtb*-infected **(d)** *B6.Sst1S* mice (n= 8) and **(e)** WT B6 old mice (n= 5) at indicated
1142 time point and treatment groups. The size of the bubble indicates %subpopulation out of
1143 all of particular cell types and color is adjusted *p* values relative to Veh group. Statistics
1144 are calculated by one-way ANOVA with Tukey's multiple comparisons test ($p > 0.15$: ns).

1145

1146

1147

1148

1149

1150

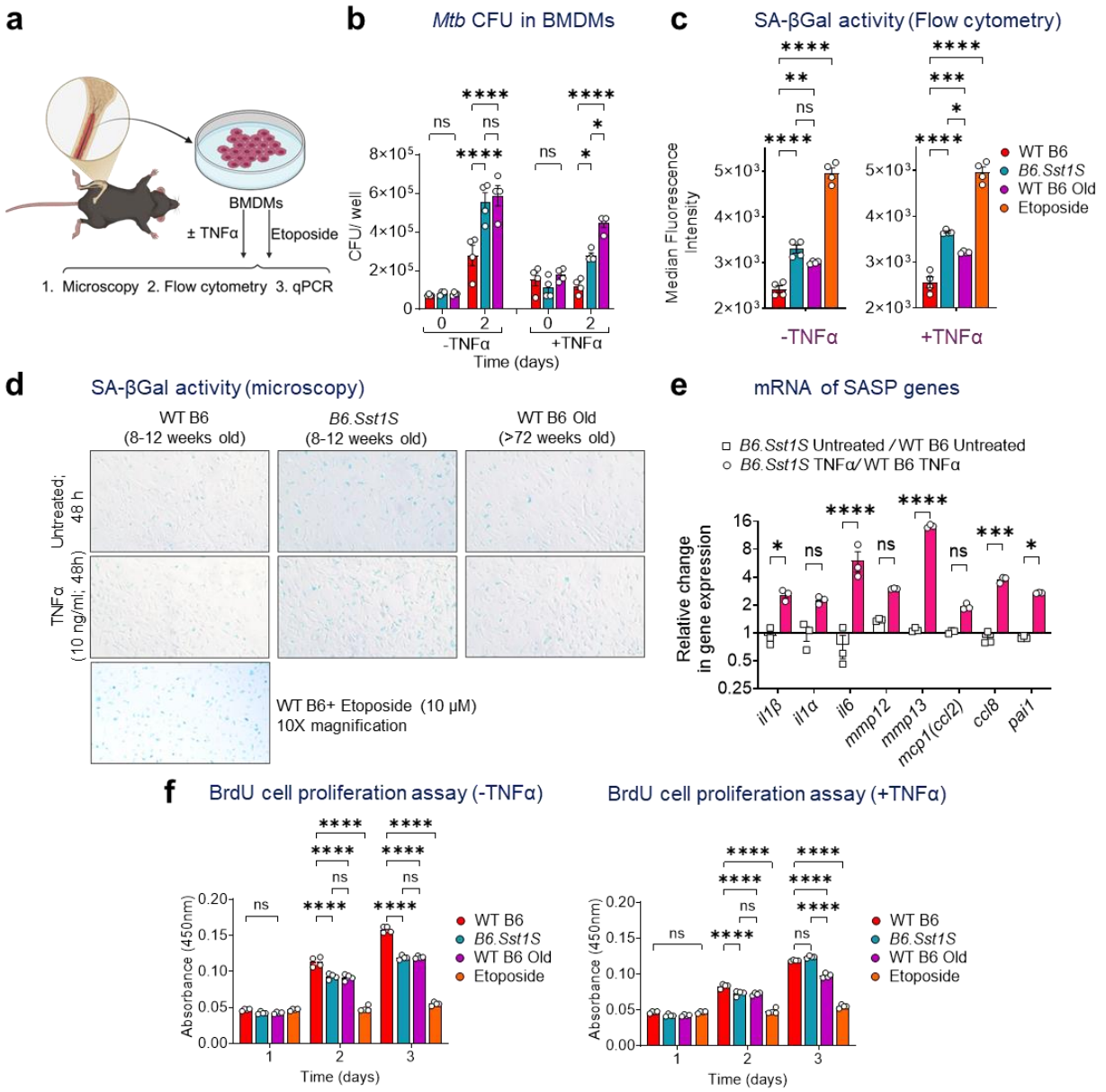


**Fig. 1. Evidence of senescence-like phenotype in BMDMs derived from young *B6. Sst1S* and aged WT B6 mice. (a)** Schematic to determine senescence associated markers in BMDMs. **(b)** BMDMs were infected for 4 hours with *Mtb* H37Rv at MOI=10, followed by removal of extracellular bacteria by extensive washing with warm media. Intramacrophage survival was determined by enumerating CFU at 2 days post-infection. The data are means ± SEM of two independent experiments (n=4). **(c)** Median Fluorescence intensity of fluorescent SA-βGal substrate by live BMDMs in presence or absence of TNFα for 48 h. 10 μM Etoposide treated WT B6 BMDMs or BMDMs from aged WT B6 mice are used as positive control. **(d)** Representative images of SA-βGal- positive BMDMs (PFA-fixed) located at the center of the TC-treated well at 20X magnification by bright field microscopy. **(e)** mRNA levels of SASP-associated genes normalized to *ActB* are shown as determined by qPCR. **(f)** BrdU incorporation by BMDMs in absence or presence of TNFα, respectively with time. The data are means ± SEM. Data is representative of two independent experiments. ($p$>0.05: non- significant (ns), $p$<0.05: *, $p$<0.01: **, $p$<0.001: ***, $p$<0.0001: ***, one-way ANOVA with Tukey's (b, c, f) or Sidak's (e) multiple comparisons test).

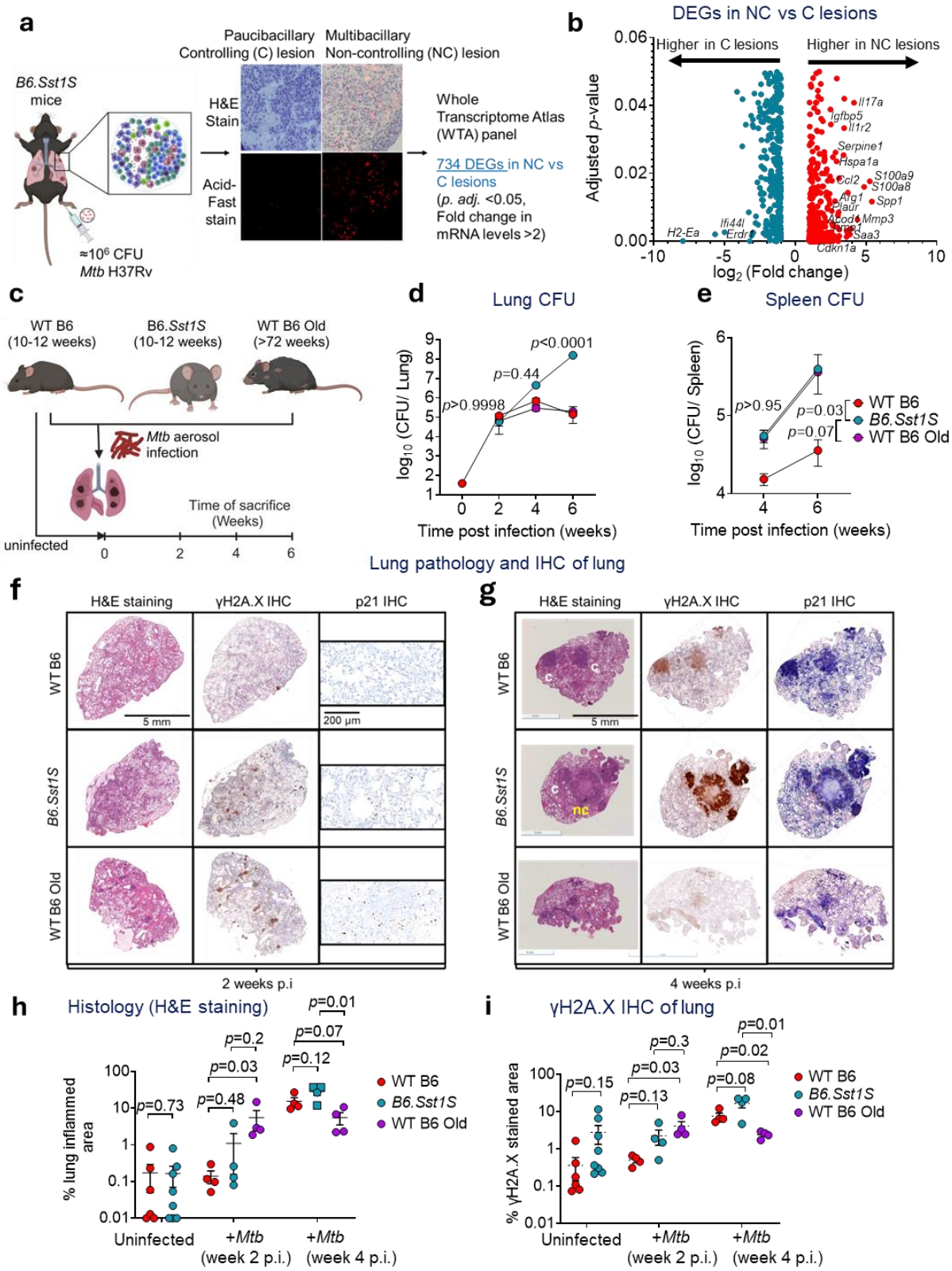


**Fig. 2. Detection of Senescence- associated markers during early stages of disease progression in *Mtb* infected mice. (a)** Schematics of Spatial transcriptomics using a Nanostring GeoMX Digital Spatial Profiler to determine differential gene expression in cells at non-controlling multibacillary granulomatous

1168 lesions (NC) relative to controlling lesions (C) in *B6.Sst1S* mice lungs. (n= 8 region of interests (ROI) from
1169 2 mice). **(b)** Volcano plot to show differentially expressed genes between controlling and non-controlling
1170 granulomatous lesions. Significantly upregulated (fold change> 2) and downregulated (fold change< 2)
1171 genes (*p.adj*< 0.05) in NC relative to C granulomas are shown in red and cyan, respectively. Top
1172 senescence associated genes in upregulated-DEGs are labelled. **(c)** Schematics of the experimental
1173 strategy to measure senescence markers *in vivo* at 2- and 4-weeks post infection (p.i.). Day1 CFU=39. *Mtb*
1174 H37Rv burden at indicated time points in WT B6, *B6.Sst1S* and WT B6 old mice **(d)** lungs and **(e)** spleen.
1175 The data are means ± SEM. Each data point represents a mouse. *p* was determined by two-way ANOVA
1176 with Tukey's multiple comparisons test. Representative H&E-stained and Immunohistochemistry against
1177 γH2A.X and p21 of mice lungs at **(f)** 2 weeks p.i. and **(g)** 4 weeks p.i. **(h)** ImageJ quantification of lung
1178 pathology (% inflamed area) in uninfected mice and *Mtb* H37Rv infected mice lungs at 2 weeks and 4 weeks
1179 p.i. (n=4-6). Squares indicate necrotic granulomas. **(i)** ImageJ quantification of γH2A.X-stained area in
1180 uninfected mice and *Mtb* H37Rv infected mice lungs at 2 weeks and 4 weeks p.i. (n=4-6). The data are
1181 means ± SEM. Each data point represents a mouse. *p* values are indicated as determined by statistical
1182 analysis between two groups as measured by unpaired two- tailed Student's t test (normal distribution) or
1183 Mann Whitney test.

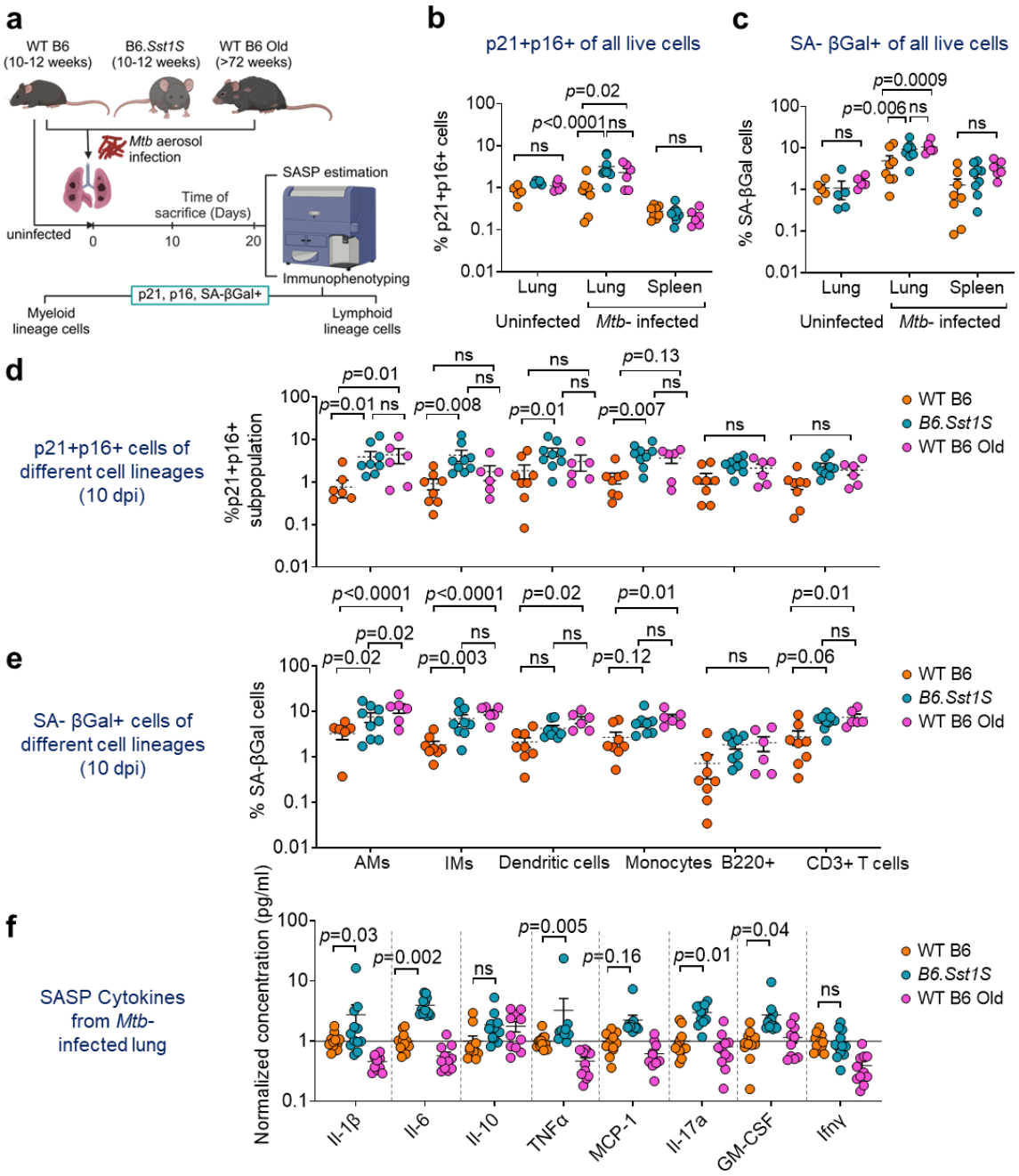


**Fig. 3. Detection of senescent cell population and SASP cytokines by flow cytometry during early stages of disease progression in *Mtb* infected mice. (a)** Schematics of the experimental strategy to measure senescence markers (p21, p16 and SA- βGal activity) and SASP cytokines levels in mice lungs at 10 and 20 days p.i. Day 1 CFU= 55. **(b)** %p21+p16+ and **(c)** %SA-βGal+ (CellEvent Senescence green+) cells out of all live lung (uninfected and *Mtb*-infected mice) and Spleen (*Mtb*-infected mice) cells at 10 days p.i. as determined by multicolor flow cytometry. **(d)** %p21+p16+ and **(e)** %SA-βGal+ cells out of different lung- cell types at 10 days p.i., as determined by multicolor flow cytometry. Gating for p16$^+$, p21$^+$, and SA-βGal$^+$ events for each cell type were established using reference cells from *Mtb*-infected WT B6 mice (set at 1 %). (AMs: Alveolar macrophages, IMs: Interstitial macrophages) **(f)** Normalized concentration of SASP-cytokines in lung homogenates at 20 dpi and 4 wpi as measured by a LEGENDplex™ Mouse Inflammation Panel (13-plex). The data are means ± SEM. Each data point represents a mouse (n=11-12). (two-way ANOVA with Tukey's (b- e) or Dunnett's (f) multiple comparisons test).

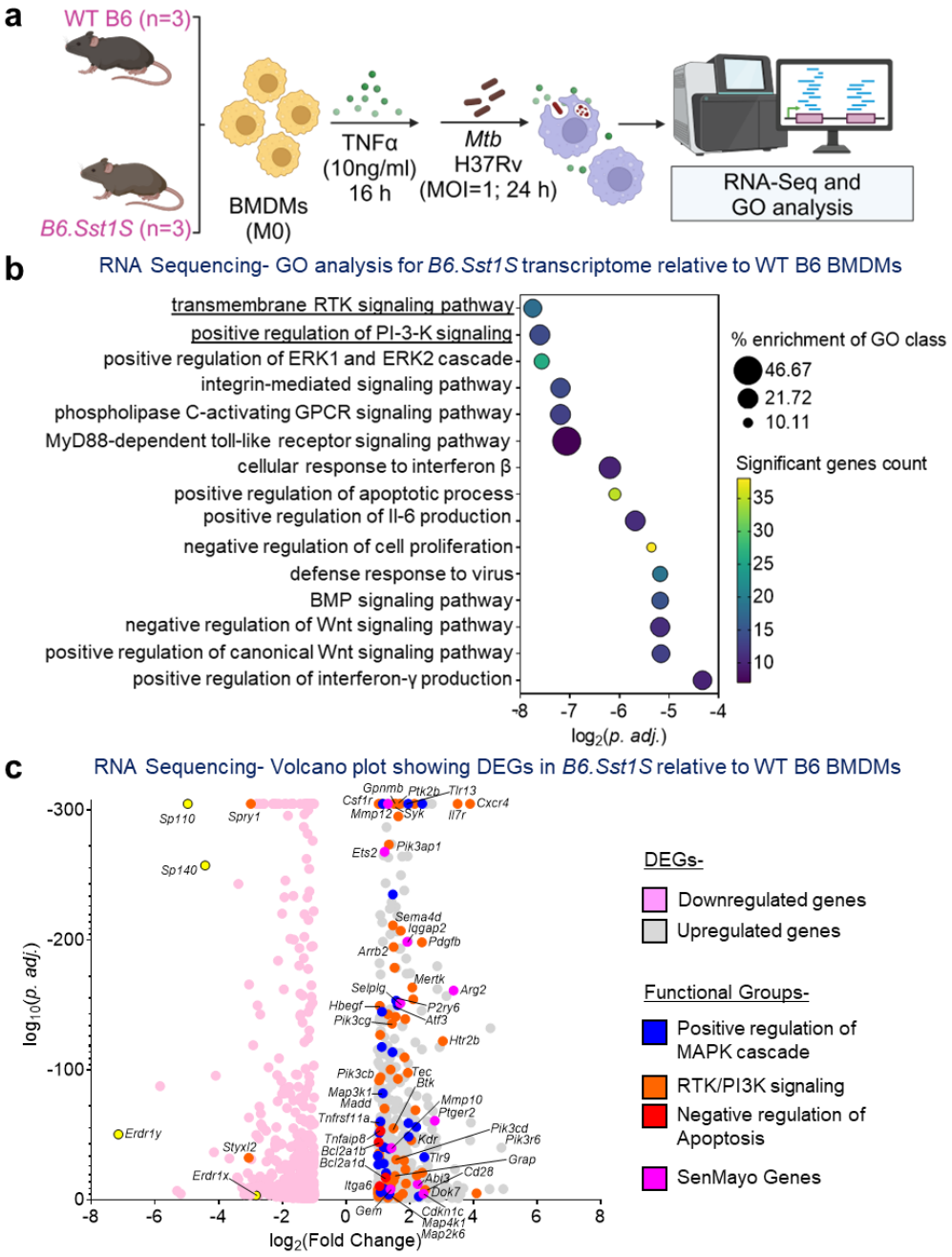


**Fig. 4. Global transcriptomics data by bulk-RNA Sequencing revealed upregulation of pro-survival pathways- PI3K-ERK1/2 and MAPK cascade in BMDMs derived from young *B6.Sst1S* relative to young WTB6 BMDMs, after treatment with TNFα and *Mtb* infection. (a)** Schematic of the experiment. **(b)** Selective representation of Gene-Ontology (GO) analysis for the differentially expressed genes (= 1177) indicating all enriched (*p.adj*< 0.05) signaling pathways. The size of the bubble indicates the percentage of DEGs out of total genes in that GO class and color indicates number of DEGs in the respective GO class. **(c)** Volcano plot of DEGs with upregulated genes in stressed (TNFα- treated and *Mtb*- infected) *B6.Sst1S* BMDMs ($log_2$ fold change >1; *p. adj.*< 0.05) shown in light gray and downregulated genes ($log_2$ fold change <1; *p. adj.*< 0.05) shown in light pink, relative to stressed WT B6 BMDMs. Genes representative of top significantly enriched GO class- Receptor tyrosine kinase signaling/ PI3K pathway (shown in orange), MAPK cascade (blue), anti-apoptotic genes (red) and SenMayo gene set (pink) are shown. Top expected downregulated genes- *Sp140* and *Sp110* are shown in yellow.

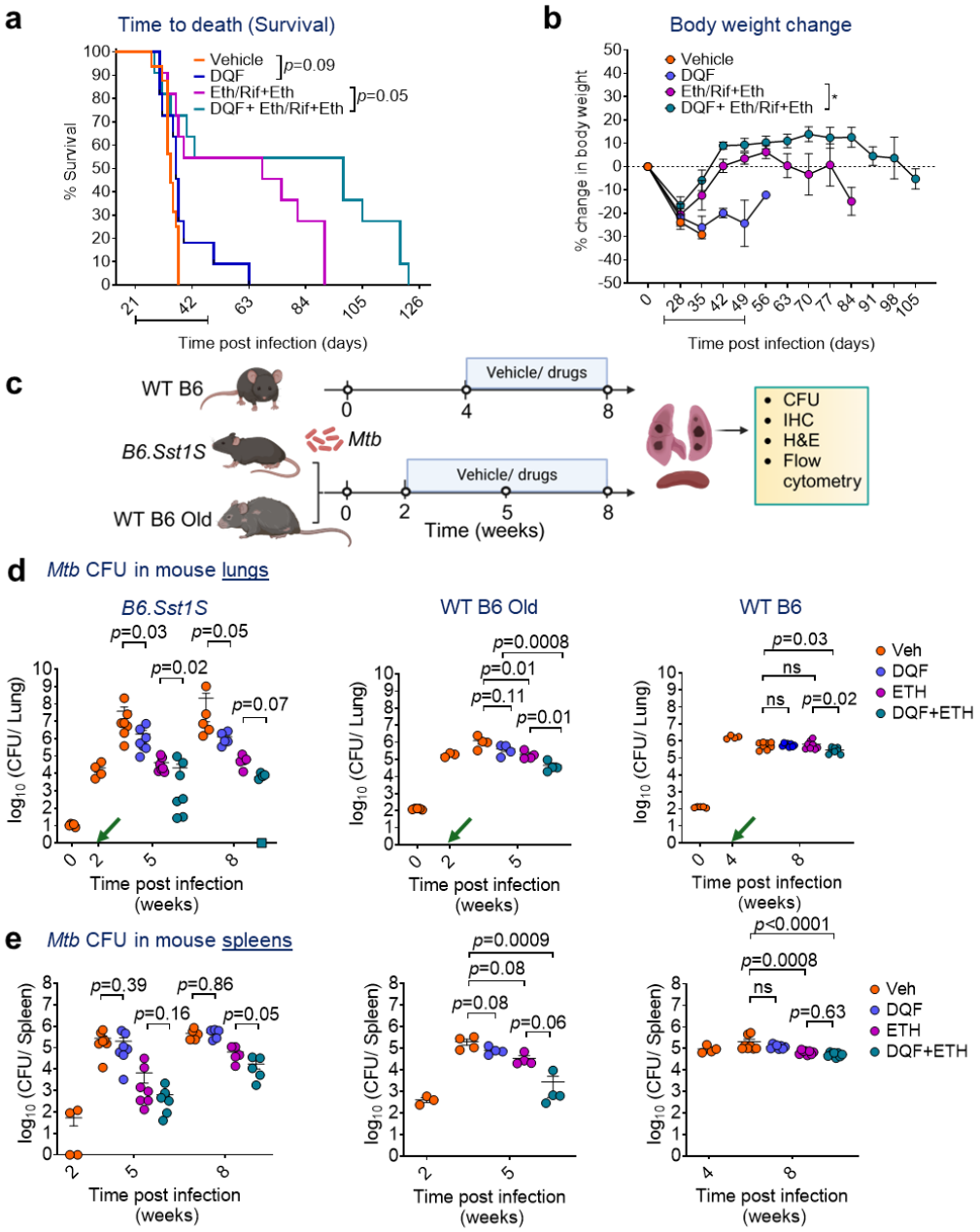


**Fig. 5. Senolytics DQF administration with or without anti-TB drug improved survival, body weight and reduced *Mtb* burden in mice. (a)** Both male and female *B6.Sst1S* mice were aerosol infected with 91 CFU of *Mtb* H37Rv and at 3 weeks p.i., mice were oral gavaged with vehicle (n=16 mice) or indicated drug regimens (n=11 mice) for the next 4 weeks. Mice were monitored for changes in body weight and survival after the start of drug treatment. **(a)** Kaplan-Meir survival curve of *B6.Sst1S* mice given varying drug regimens. Line indicates duration of oral gavage therapy. Indicated *p* values are measured by log-rank (Mantel-Cox) test. **(b)** Changes in body weight are plotted as a % change in body weight of surviving mice relative to Day 1 p.i. over time. The data are means ± SEM. ($p<0.05$: *, two-way ANOVA with Tukey's multiple comparisons test). **(c)** The experimental strategy. Day 1 CFU in *B6.Sst1S* mice= 11; WT B6 young and old mice= 126. *Mtb* H37Rv burden in **(d)** lung and **(e)** spleen of *B6.Sst1S* (left), old WT B6 mice (center), and WT B6 (right), at indicated time points (n=4-7). Square indicates CFU below the limit of detection (=10). The green arrow indicates the start of drug treatment. The data are means ± SEM. Statistical analysis between two groups was done by unpaired two- tailed Student's t test.

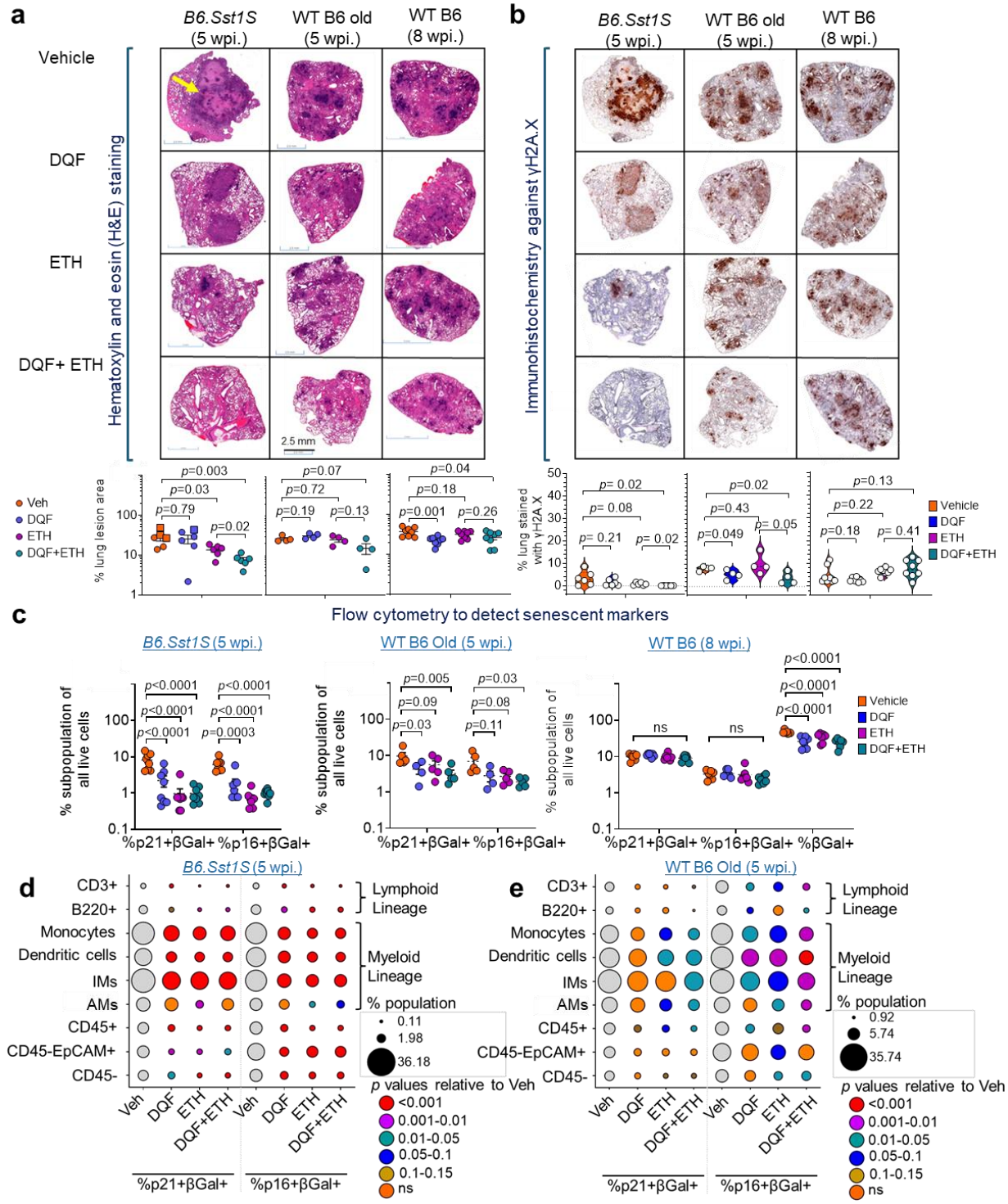


**Fig. 6. Senolytics administration alone, and in combination with ethambutol reduced lung pathology and senescence-associated markers in *Mtb* H37Rv infected *B6.Sst1S* and WT B6 old mice. (a)** Representative H&E-stained images of *Mtb*-infected mice lungs treated with Vehicle or drugs, and respective ImageJ-based quantification. Yellow arrow indicates necrotic granuloma in Vehicle treated *B6.Sst1S* mice at 5 wpi. The data are means ± SEM. Each data point represents a mouse. Statistical analysis between two groups was done by unpaired two- tailed Student's t test. Square represents necrotic

1228 granuloma formation in the lung. **(b)** Representative γH2A.X- Immunohistochemistry images of mice after
1229 lungs vehicle/ drugs treatment, and respective Violin plots to show ImageJ quantification of γH2A.X-stained
1230 area. Each data point represents a mouse. Statistical analysis between two groups was done by unpaired
1231 two- tailed Student's t test. **(c)** %p21+βGal+ and %p16+βGal+ subpopulation observed in all live lung cells
1232 of *Mtb*-infected mice (n= 5-8). The data are means ± SEM. Each data point represents a mouse. Statistical
1233 analysis was calculated by two-way ANOVA with Dunnett's multiple comparisons test.

1234 Bubble plot to show %p21+βGal+ and %p16+βGal+ subpopulation in different lung cell types in *Mtb*-
1235 infected **(d)** *B6.Sst1S* mice (n= 8) and **(e)** WT B6 old mice (n= 5) at indicated time point and treatment
1236 groups. The size of the bubble indicates %subpopulation out of all of particular cell types and color is
1237 adjusted *p* values relative to Veh group. Statistics are calculated by one-way ANOVA with Tukey's multiple
1238 comparisons test ($p > 0.15$: ns).